Fall 12-18-2018

Noise and Gain Characterization of Interband Cascade Infrared Photodetectors

Eli A. Garduño
University of New Mexico

Eli A. Garduño

Candidate

Electrical & Computer Engineering

Department

This dissertation is approved, and it is acceptable in quality and form for publication:

Approved by the Dissertation Committee:

Dr. Ganesh Balakrishnan , Chairperson

Dr. Christian Morath

Dr. Adam Hecht

Dr. Francesca Cavallo

Noise and Gain Characterization of Interband Cascade Infrared Photodetectors

by

Eli Alan Garduño

B.S., Physics, U.S. Air Force Academy, 2012
M.S., Applied Physics, Air Force Institute of Technology, 2014

DISSERTATION

Submitted in Partial Fulfillment of the
Requirements for the Degree of

Doctor of Philosophy
Electrical Engineering

The University of New Mexico

Albuquerque, New Mexico

May 2019

Acknowledgments

Foremost, I would like to thank Dr. Christian Morath for persistently challenging and supporting me in this research. I am immensely grateful for your willingness to drop other tasks in order to help me in the lab and to entertain discussions of the physics driving the results. I would also like to thank Dr. Vincent Cowan, Dr. Elizabeth Steenbergen, and Dr. John Hubbs for imparting on me a portion of their expertise in infrared detector development and testing. Furthermore, I would like to extend thanks to all members of the Air Force Research Lab Advanced Electro-Optic Space Sensors Group whose dedication inspired me and whose efforts made my research possible. I would also like to thank my former and current advisors, Dr. Sanjay Krishna and Dr. Ganesh Balakrishnan, who guided me in shaping my topic and who helped me work around other professional demands to complete this research. In addition, I owe thanks to Dr. Rui Yang and his team at University of Oklahoma for their collaboration. I also owe thanks to the outstanding summer scholars I have had the privilege to work with and mentor over the past several years. I would also like to thank my parents for imparting on me their different strengths and for encouraging me every day of my life. Finally, I would like to thank my wife for unceasing support and love through the highs and lows of this research and beyond. Without those mentioned above and many others, this work would not have been possible. Thank you.

Noise and Gain Characterization of Interband Cascade Infrared Photodetectors

by

Eli Alan Garduño

B.S., Physics, U.S. Air Force Academy, 2012
M.S., Applied Physics, Air Force Institute of Technology, 2014
Ph.D., Electrical Engineering, University of New Mexico, 2019

Abstract

Infrared (IR) detectors are an enabling technology for a broad and growing list of applications including gas detection, night vision, and space-based missile warning. There are ongoing efforts in IR detector research to explore the potential of new material systems and energy band structures in addition to continuously improving their sensitivity through increasing their quantum efficiency and lowering their dark current and noise. This dissertation examines an emerging class of IR detectors known as Interband Cascade Infrared Photodetectors (ICIPs).

ICIPs contain multiple regions to facilitate the collection of photogenerated electrons and to limit unwanted dark current. Theory regarding their performance also indicates that multi-stage ICIPs may have lower noise than single-stage ICIPs and may provide improved detectivity in cases where the absorption coefficient of a material system is small and/or where the diffusion length in the material is short or degraded.

In this work, four long-wavelength infrared ICIP devices with one, four, six, and eight stages were characterized at varying temperatures from 80 to 300 K and at biases up to one volt in both forward and reverse polarities. Noise spectra were collected on the four devices and show significant $1/f$ noise that prevented direct measurement of the ICIP noise gain. The $1/f$ noise in the ICIPs was correlated to generation-recombination current. The devices were found to cause circuit instability when operated in bias regions with negative differential conductance (NDC) due to bias-dependent resonant tunneling. Additionally, bias-dependent photocurrent gain was observed using illumination of the devices with 632 nm and 1550 nm lasers which peaked near the NDC regions. This photocurrent gain was experimentally shown to be linked to current-mismatch between device stages, supporting theories regarding its origin.

Contents

List of Figures

Chapter 1

Introduction

1.1 Infrared Radiation and Applications

For millenia, human visual perception was limited by our eyes which are capable of detecting only a small portion of the electromagnetic (EM) spectrum. The "visible spectrum" to which the human eye is sensitive spans only the wavelength range from about 390 nm to 780 nm. Beyond 780 nm to about 1 mm lies the infrared (IR) spectrum.[1] The IR spectrum contains a vast amount of information about material properties and can be used to see objects when no visible light source is available to provide illumination. The invention and continual advancement of IR detector technology has allowed us a completely new perspective on the world and has opened up an ever-growing list of commercial and military applications using terrestrial and space-based platforms.

One key component to understanding the utility of using IR radiation for sensing and imaging is understanding Planck's Law. In 1900, Max Planck formulated a function to relate the radiation density emitted by an object to its temperature. He developed what came to be known as Planck's Law given in terms of spectral

exitance for a blackbody with unity emissivity as[2]

$$M_q(\lambda, T) = \frac{2\pi c}{\lambda^4(e^{hc/\lambda kT} - 1)} \tag{1.1}$$

where M_q is given in units of photons/s cm$^2\mu$m, T is the object temperature, h represents Planck's constant = 6.626×10^{-34} J s, λ is the wavelength of the EM radiation, c is the speed of light = 2.99×10^8 m/s, and k is Boltzmann's constant = 1.381×10^{-23} J/K. Plotting equation 1.1 for a variety of objects with vastly varying temperatures in figure 1.1 shows one of the most important features of the law, namely that the peak spectral emission occurs at shorter wavelengths for hotter objects and longer wavelengths for cooler objects. Objects at different temperatures will not only radiate different amounts of photons, the ratios of photons at various wavelengths will change. Therefore, applications seeking to image or sense objects in different temperature regimes rely on IR detectors sensitive to a specific band of the IR spectrum.

Nomenclature with varying conventions has been developed to further describe portions of the IR spectrum. Roughly speaking, the near-infrared (NIR) spans 780 nm to 1 μm, the shortwave IR (SWIR) spans 1 to 2.5 μm, the midwave IR spans 2.5 to 7 μm, and the longwave IR (LWIR) spans 7 to 14 μm.[1, 3] Detectors fabricated using a variety of materials have been developed to sense in these different regimes, leveraging multiple quantum mechanical principles. Infrared detectors are used for a variety of tasks including night vision imaging, gas detection, missile detection and tracking, security screenings, electrical diagnostics, and many more. Improvements in these application fields come from advancements in optical sciences and image processing. The performance of the IR detectors used often limits the utility of the whole system. With this in mind, research is ongoing to increase the performance of IR detectors on multiple fronts.

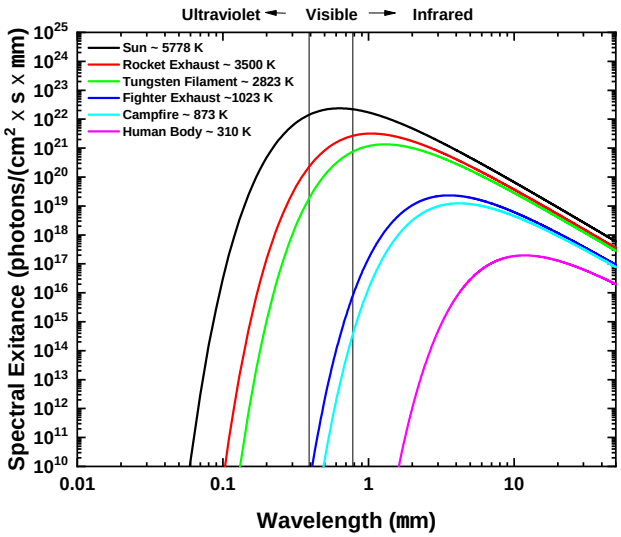

Figure 1.1: Spectral exitance of different objects showing that hotter objects not only emit more photons but also emit the majority of their photons at shorter wavelengths.

1.2 Motivation and Approach

Two key thrusts in improving IR detectors are in increasing the signal; the measure of how well a detector converts photons to electrons, and decreasing the noise; a measure of the undesired current produced by a detector that can mask the photogenerated current. Both parameters will be discussed in more detail in chapter 2. Generally, the signal is dictated by the quantum efficiency of a device and the noise is dictated by the dark current. If the dark current were constant in time, it could be easily subtracted out from the overall current to reveal just that generated by incoming photons. Unfortunately, the dark current varies in time and the magnitude of those variations can make it difficult to distinguish the signal from the noise. Noise is typically quantified in terms of the root-mean-square (rms) deviation of the current or voltage from the mean value.[2] Noise is a function of frequency bandwidth and is reported in terms of spectral density in which the total rms value is

normalized by the square root of the bandwidth. The units of noise are then typically reported as $A/\sqrt{Hz}$ or $V/\sqrt{Hz}$. IR detector noise can be measured through multiple methods and is reported on through multiple figures of merit discussed further in chapter 2. In many cases in both the literature and in commercial development, however, noise is simply estimated using the measured dark current value. In this work, multiple detector types were tested under differing operating conditions to find those under which noise estimation is more or less reliable and to relate certain noise features to physical phenomena in the detectors. The overarching goal was to experimentally determine the theoretical noise gain of interband cascade infrared photodetectors (ICIPs) and to validate physical explanations for additional noise and gain mechanisms in actual devices. Other detector types are used for comparison and to explore different current mechanisms and operating regimes relevant to the operating principles of ICIP devices.

1.3 Overview of the Dissertation

The remainder of the document is organized into chapters that build on one another. Chapter two provides an introduction to photovoltaic IR detectors in a broad sense including the physics relevant to one of the simplest photovoltaic detectors, the photodiode. Different current mechanisms relevant to the work are explained. Building on the discussion of the diode, the nBn and interband cascade infrared photodetector (ICIP) architectures are introduced as well as those of relevant devices such as the resonant tunneling diode (RTD) and the four-zone quantum well infrared photodetector (QWIP). The operating principles and unique characteristics of the ICIP architecture are discussed in depth, drawing on some of the physics of the other devices. Chapter two also includes an introduction to the primary performance metrics used in assessing IR detectors and then wraps up with an introduction to detector

noise sources and theory.

Chapter three sets the stage for the findings of this work by explaining the specific detector architectures tested and experiments performed. The chapter also provides information on the multiple test apparatuses used and the upgrades that were made in the process of this work.

Chapter four comprises the bulk of the document and lays out the radiometric and noise characterization results from testing an nBn detector both pre- and post-irradiation by a 63 MeV proton source and from testing a set of ICIP devices with varying numbers of stages. The nBn results serve in some aspects as control data for the exploration of the more exotic ICIP architecture testing.

The final chapter recaps the initial goals of this work and summarizes the findings in the context of those goals, highlighting the findings most novel and relevant to the IR detector research community. From there, the document wraps up with recommendations for further experimentation informed by the findings of this work.

Chapter 2

Theory and Background

2.1 Types of IR Detectors

There are two primary ways of detecting IR radiation. The first is by creating a device that changes temperature in response to incident IR radiation due to the heat it is absorbing. These devices are known as thermal detectors. The temperature is associated with a measurable change in other parameters of the device. Examples of thermal detectors include Bolometers in which temperature changes resistance, pyroelectrics in which temperature changes material polarization, and thermocouples in which temperature changes voltage.[3]

The second type of IR detector takes advantage of the quantized nature of electromagnetic radiation through the detection of photons. An incident photon in a semiconductor with enough energy causes an electron to be excited from the valence energy band wherein it is still bound to its atom to the conduction energy band where it is free to flow through the material as current. Photon detectors rely on this property to detect incident photons and can be further divided into two main categories; photoconductors and photovoltaic detectors. As photons excite electrons

in the former, the conductivity across the device is altered and can be monitored to determine the incident photon flux. In the latter, the increase in charge carriers generates an increase in either current or voltage which can be monitored as the device signal. The types of detectors in this work are all of the photovoltaic variety. While this work focuses on nBn and interband cascade infrared photodetectors (ICIPs), additional detector types will be discussed for their relevant physics including the p-n junction photodiode, four-zone quantum well infrared photodetectors (QWIPs), and resonant tunneling diodes (RTDs). The physics of the p-n junction appears in many more complicated devices because their architectures typically necessitate one or more junctions of material with different dopant types or concentrations. QWIPs, and in particular four-zone QWIPs, are discussed to relate their similarities with ICIPs and to draw from related characterization work in the literature. RTDs are discussed in the context of negative differential conductance as the resonant tunneling physics proves relevant to the ICIP devices' dark current characteristics as well as their interaction with other circuit elements in the test apparatus.

2.2 Photodiode

The simplest photovoltaic IR detector is a p-n junction diode. The junction is formed at the interface between a p-type material and an n-type material. The p-type semiconductor has atoms that prefer to have more electrons to get close to a filled valance shell while n-type semiconductors are those that prefer to give up electrons to get closer to eliminating the partially filled valence shell. When they come into contact, electrons from the n-type region diffuse into the p-type region and holes diffuse from the p-type region to the n-type region. The diffusion process is dictated by the concentration gradient of carriers throughtout the regions and the interface.

The diffusion rates of the two carriers in terms of current density are represented by

$$J_{n,diff} = qD_n \frac{dn(x)}{dx}, J_{p,diff} = -qD_p \frac{dp(x)}{dx}, \tag{2.1}$$

where q is the elementary charge, D_n and D_p are the diffusion coefficients for the electrons and holes respectively and $n(x)$ and $p(x)$ are the concentrations of the electrons and holes as a function of position, x, respectively.[4]

As the electrons and holes diffuse across the junction, they leave behind their constituent atoms that are still bound in the semiconductor lattice. Now missing their electrons and holes, these ions have a net charge. Therefore, near the junction, the donor atoms, having given up electrons, then have a positive charge. Likewise, the acceptor atoms, having given up holes by accepting electrons, now have a negative charge. The cumulative effect of the charge separation between the ionized acceptors on the p-type side of the junction and the ionized donors on the n-type side of the junction is the formation of an electric field across the region depleted of the free carriers, also known as the depletion region.

As carriers enter the depletion region, the electric field exerts a force causing the electrons to move back toward the n-type side of the junction and the holes to move back toward the p-type side of the junction. The current caused by this electric field is called the drift current. Expressed in terms of the current density, the drift current is give by

$$J_{drift} = q(n\mu_n + p\mu_p)E, \tag{2.2}$$

where μ_n and μ_p represent the electron and hole mobilities respectively and E represents the electric field.[4]

The two current mechanisms cause carriers to move in opposite directions, reaching an equilibrium wherein the width of the depletion region, absent an external bias and excluding small fluctuations, becomes a constant.

Introducing an external electric field can further influence the net current flow and the width of the depletion region. A bias applied such that the resultant electric field is in the same direction as that generated by the separation of charges in the depletion region is known as a forward bias. A forward bias makes it more difficult for carriers to diffuse from one side of the junction to the other and hence, decreases the depletion width. A bias applied in the opposite direction as the built in electric field compliments the diffusion process and creates an even larger depletion region. Once the junction is formed, the current is limited by the diffusion of carriers from the quasineutral regions to the junction boundaries. The gradient of carriers at the junction boundaries is a function of the carrier concentrations, the diffusion lengths, and the electric field across the junction. The electrical field can be increased or decreased through the application of an external bias. The p-n junction then becomes a detector by applying electrical contacts on the different sides of the junction.

The ideal current i of the resulting photodiode is given by

$$i = i_0(e^{qV/kT} - 1), \tag{2.3}$$

where i_0 is the reverse saturation current defined by

$$i_0 = q(\frac{n_p D_e}{L_e} + \frac{p_n D_h}{L_h})A_d, \tag{2.4}$$

in which L_e and L_h are the diffusion lengths of the electrons and holes respectively given by $L_e = \sqrt{D_n \tau_n}$ and $L_h = \sqrt{D_p \tau_p}$.[4]

As photons are absorbed in the depletion region, the charge carriers they excite from the valence into the conduction band are swept out of the junction by the

electric field. Once in the neutral region they, along with any carriers generated outside of the junction, diffuse to the contact and are allowing them to be collected as current. This additional photogenerated current, i_{ph}, becomes a constant offset to the current given by equation 2.3 so that the illuminated photodiode current is given by

$$i = i_0(e^{qV/kT} - 1) - i_{ph}. \tag{2.5}$$

If no bias is applied, this additional current is known as the short-circuit current. If a forward bias is applied, it will detract from the photogenerated current. At a certain bias - the open-circuit voltage - there will be no current through the device. If no current is allowed to flow by operating the photodiode in an open-circuit configuration (applying enough bias in the forward direction to zero out the net current), the separated charge creates a voltage across the device.

Other currents such as G-R currents can exist in photodiodes. These additional current mechanisms may contribute in unique ways to the detector noise so their physical explanations are discussed here. The mechanisms covered include G-R through multiple physical processes, interband tunneling, and trap-assisted tunneling. Intraband tunneling will be further discussed in the sections explaining the operating principles of QWIPs and ICIPs.

2.3 Other Current Types

As its name implies, Generation-Recombination (G-R) currents occur when excess carriers are generated through processes other than radiative excitation or when carriers recombine. Carriers can be generated through thermal excitation. The proba-

bility of electrons occupying energy states is given by the Fermi-Dirac distribution

$$f_D(E) = \frac{1}{1 + exp[(E - E_f)/kT]}, \tag{2.6}$$

where E_f is the Fermi energy or Fermi level where the probability of occupancy equals 1/2. Whether states are available to be occupied is determined by the density of states $g(E)$ so that the density of electrons in the conduction band, n is given by

$$n = \int_{cb} f_D(E)g(E)dE. \tag{2.7}$$

Equation 2.6 can be simplified in cases where the Fermi level is much below the conduction band, where $(E_C - E_f) >> kT$. In this case, Maxwell Boltzmann statistics apply due to the negligible effect of the Pauli-Exclusion principle in the mostly unoccupied conduction band states so that

$$f_M(E) = exp[\frac{-(E - E_f)}{kT}]. \tag{2.8}$$

Using this in equation 2.7 and using N_c as the effective density of states in the conduction band, the concentration of electrons in the conduction band becomes

$$n = N_c exp[-\frac{(E_c - E_f)}{kT}]. \tag{2.9}$$

N_c is given by

$$N_c = 2(\frac{2\pi m_n * kT}{h^2})^{3/2}, \tag{2.10}$$

where m_n* is the effective mass of electrons. From equations 2.11 and 2.12, one can see that as the temperature increasing both N_c and f_M increase which dictates that

more electrons will be present in the conduction band. A formulation analagous to that above can be shown for the concentration of holes in the valence band, p wherein

$$p = N_v exp[-\frac{(E_f - E_c)}{kT}], \tag{2.11}$$

and N_v, the effective density of states in the valence band is given by

$$N_v = 2(\frac{2\pi m_p * kT}{h^2})^{3/2}. \tag{2.12}$$

Since the effective densities of states and f_M increase with temperature, it is apparent that an increase in temperature will result in more holes in the conduction band and electrons in the valence band. Once there, these electrons and holes act no differently than electron-hole pairs generated by the absorption of a photon and thus, contribute to the unwanted dark durrent. Similarly electrons can relax down from the conduction band to the valence band and either emit a photon or impart their energy to another electron in the the conduction band. These recombination processes are known as radiative recombination and Auger recombination respectively.

In addition to thermal excitation, electrons and holes can be generated with help from energy states that exist within the forbidden energy gap due to localized defects and impurity atoms. Electrons can either be captured by these local states or excited from the states into the conduction band. Similarly, holes can either be captured from the valence band (an electron relaxing into the valence band) or holes can be generated in the valence band by electrons exciting into the intraband states. These four processes are collectively called Shockley-Read-Hall recombination. The recombination rate, U is given by

$$U = \frac{n_i^2(e^{qV_a/kT} - 1)}{(p + n + 2n_i cosh\frac{(E_t - E_i)}{kT})\tau_0}, \tag{2.13}$$

where V_a is the applied bias, E_t is the energy level of the trap, E_i is the intrinsic Fermi energy level near the middle of the bandgap, and τ_0 is the SRH carrier lifetime.

For a p-n junction in forward bias (V_a is positive), the recombination rate is postive as carriers can more easily enter the depletion region and recombine, conbributing a positive current. In reverse bias, carriers generated in the depletion region are quickly swept out by the high electric field, causing an increase in the negative current.

Besides being able to recombine and generate through trap states in the bandgap, electrons in the valence band can sometimes tunnel straight through the forbidden gap to the conduction band. This process is known as interband tunneling. As a reverse bias is applied to a p-n junction, the depletion width decreases and electrons on the p-side of the junction become spatially closer to vacancies sharing their same energy level on the n-side of the junction. The probability that the elecron will tunnel through the gap is approximated by

$$P_t = exp(-\frac{qBW_{dep}}{E_g}), \tag{2.14}$$

where the potential barrier, B, that the electron must tunnel through is given by

$$B = \frac{4\sqrt{2m^*}E_g^{3/2}}{3q\hbar} \tag{2.15}$$

so that as the depletion width decreases or the bandgap decreases, the probability of tunneling increases.[5] Thus, tunneling is expected to manifest at higher reverse biases and in materials designed for longer wavelength IR detection with a smaller bandgaps.

When trap states are present in the bandgap, electrons can cross the gap through a combination of tunneling and thermal excitation to and from the intraband states. This process is known as trap-assisted-tunneling (TAT).

Resonant tunneling is an additional tunneling mechanism wherein structures with multiple quantum wells are more transmissive to electrons with specific energies due to alignment of bound energy levels in the wells. This makes the multi-well structure more transmissive to incident electrons than the individuals barriers alone.[6]

2.4 nBn Photodetectors

As discussed above, the p-n photodiode must contend with unwanted dark current due to SRH generation in the depletion region and diffusion currents resulting from radiative and Auger recombination. Currents at surface interfaces and boundaries can also contribute unwanted current but are not discussed here. In 2006, Maimon and Wicks reported on the development of the nBn photodetector that claimed to significantly limit the SRH and surface currents compared to traditional p-n photodiodes.[7] As its name implies, the nBn detector uses a wide bandgap material between two n-type regions, one as the contact layer and the other as the absorbing layer. Figure 2.1 below shows the band diagram of a simple nBn. A photogenerated electron in the absorbing layer diffuses to the contact layer on its side of the barrier, while its complimentary hole diffuses and drifts to the contact on the opposite side of the barrier.

In a p-n structure depletion region, midgap traps are activated and the SRH generation current is proportional to the depletion width, W_{dep} with

$$J_{SRH} \approx q\frac{n_i}{\tau_{SRH}}W_{dep}, \tag{2.16}$$

where n_i is the intrinsic carrier density and τ_{SRH} is the SRH recombination lifetime. In an nBn, most of the depletion region is contained in the barrier where the large energy gap significantly reduces SRH recombination. The nBn still has diffusion

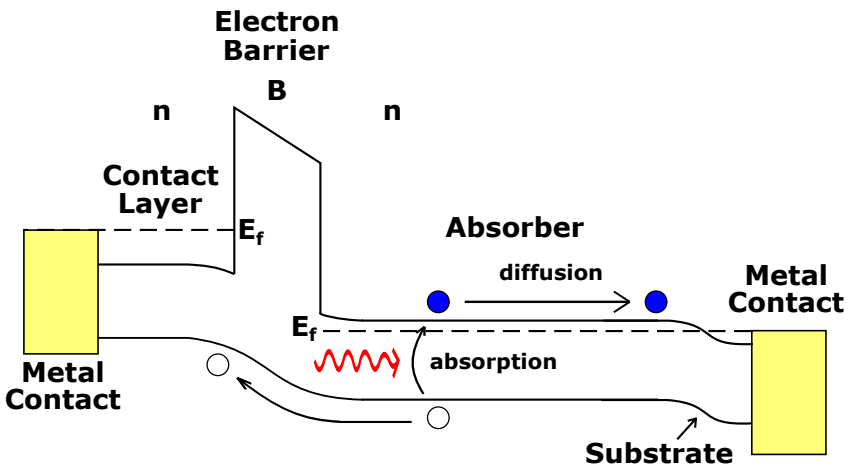

Figure 2.1: Band diagram of a reverse-biased nBn photodetector.

dark current given by

$$J_{diff} \approx q\frac{n_i^2}{N_d}\frac{1}{\tau_{diff}}L, \tag{2.17}$$

where τ_{diff} is ideally the Auger or radiative limited lifetime. Comparing equations 2.16 and 2.17, one can see that the nBn is expected to be diffusion limited where $n_i^2/N_d > n_i$ when the neutral region is extrinsic.[7] In addition to reducing SRH, the barrier acts as a passivation layer atop the active absorbing layer and thus reduces the surface current.

Unlike in a p-n junction where the photocurrent is swept out of the depletion region by the electric field, in an nBn the minority holes diffuse past the barrier.

2.5 Interband Cascade Infrared Photodetectors

In 2005, around the same time as the nBn devices were first being developed, interband cascade infrared photodetectors (ICIP) were created using the energy

band structure of interband cascade lasers (ICL).[8] The earliest reported experiments on ICIPs used as-grown ICL wafers processed into mesa waveguide lasers and mesa geometry photodetectors with room temperature cutoff wavelengths of 3.3 μm and 4.4 μm respectively. The mesa waveguide lasers and mesa photodetectors demonstrated room temperature, Johnson-noise limited detectivities of 1.4×10^9 cm $\mathrm{Hz}^{1/2}$/W and 7.1×10^8 cm $\mathrm{Hz}^{1/2}$/W respectively which approached commercial PbSe photoconductors at the time of publication.[8] Multiple advancements in both the performance and physical understanding of ICIPs have been made since. The external quantum efficiency of ICIPs is limited by the number of stages, however, their multi-stage architecture offers potential benefits for applications demanding high-speed response or where the absorption coefficient and/or the diffusion length is particularly small.[9] Multi-stage ICIPs also offer low noise compared single-stage devices due in part to their lower dark current and higher resistivity. Theory also suggests that multi-stage devices may have noise below the single-stage shot-noise limit due to the fact that electrons transiting the device in separate stages constitute separate events akin to adding trials in an experiment.[10] This section will discuss the basic operating principles, advancements, and some remaining questions about the devices.

2.5.1 Basic ICIP Architecture

The basic stage of an ICIP contains three regions: (1) an absorbing region; (2) an electron relaxation region which doubles as a hole barrier; and (3) an interband-tunneling region which doubles as an electron barrier. The absorber, the electron relaxation and the interband-tunneling regions are analogous to the active lasing region, the electron injection and hole injection regions in an ICL, respectively. Figure 2.2 shows a simplified energy band diagram for a single stage of an ICIP. The relaxation region in the ICIP is made of quantum wells that increase in width fur-

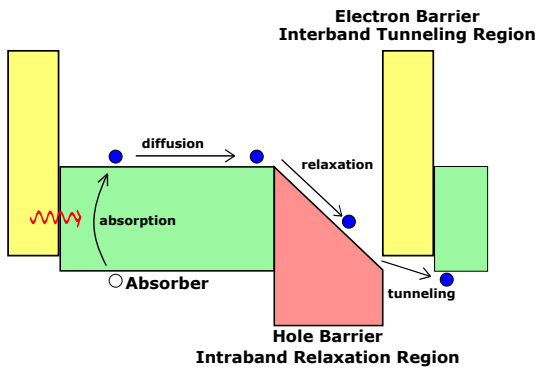

Figure 2.2: Energy band diagram of a single stage of an ICIP.

ther from the absorber such that their ground state energies form a staircase down from the absorber toward the valence band of the electron barrier. After an electron diffuses to the edge of the absorber, where it meets the relaxation region, it will continually seek lower energy states. This natural relaxation in energy drives physical transit of electrons through the device. The relaxation region acts as an electric field, sweeping the carriers out of the edge of the absorber which further fuels a carrier concentration gradient, allowing diffusion to continue in the asbsorber toward the relaxation region. In a multi-stage ICIP, the end of the relaxation region in each stage is designed to have a final quantum well ground state energy near the valence band of the next absorbing region so that it can efficiently tunnel into the next stage, recombining with a hole. The carrier transport mechanism described above does not rely on an external bias. This allows ICIPs to operate at or near zero-bias. Low-bias operation can lower the power requirement of a single detector or focal plane array. Additionally, near zero-bias, the device dark current is at its lowest. This can reduce dark current induced shot noise but a lower differential resistance at zero-bias also increases the Johnson noise.

2.5.2 Multi-Stage ICIP Tradeoffs

The single-stage of an ICIP can be repeated in a semiconductor layer stack so that a device has multiple absorbing regions. After an electron tunnels from one stage into the valence band of the absorption region, it is inhibited from further transport through the device. However, if it absorbs an additional photon or is excited to the conduction band through SRH or thermal excitation, the transit process may continue with diffusion, relaxation and tunneling into the next stage where the whole process repeats. Thus, in a multi-stage ICIP architecture, each stage must absorb a photon in order for full transport of a photogenerated carrier. In an ICL, an electron that fully transits the device must undergo radiative relaxation as many times as there are stages so the number of photons emitted per electron can be greater than one. For the ICIP, the opposite is true so that the external quantum efficiency is bounded by the number of stages ($\eta_{ext} \leq 1/N_s$ where N_s is the number of stages).

Generally, IR detectors are designed in part to maximize the number of electrons generated by a given photon and collected. Thus, it seems counterintuitive to explore an infrared detector architecture that requires multiple photons in order for one electron to be collected in the external circuit. There are cases, however, where single-stage devices run up against performance constraints of their own and where multi-stage ICIPs may offer some advantages. Multiple theoretical analyses have been used to determine that multi-stage devices offer advantages when the product of the absorption coefficient, α, and the diffusion length, L, is small.[9, 10]

Starting in the simple case for an absorber of length d with zero surface recombination velocity and no electric field (flat band absorber), the total current collected will be influenced by the generation rate $g(x)$ at a distance x from the collection point and the probability that a carrier generated at x will be collected before recombining represented as $f_c(x)$. This is true for both thermally generated carriers and those

resulting from photon absorption. Integrating the product of these two terms over the absorber length yields the total current collected from the absorber[10]

$$I_{coll} = \int_0^d f_c(x)g(x)dx, \tag{2.18}$$

The absorption coefficient directly drives the photogeneration rate, $g_{ph}(x)$ at distance x into the material by the relation[5]

$$g_{ph}(x) = g_0 e^{-\alpha x}, \tag{2.19}$$

where g_0 is a material dependent constant. In the flat band case with zero recombination velocity, $f_c(x)$ is driven by the diffusion length such that[10]

$$f_c(x) = \frac{cosh[(d-x)/L_n]}{cosh(d/L_n)}. \tag{2.20}$$

From equation 2.19 it is apparent that if the absorption coefficient is small, $g_{ph}(x)$ decays more slowly as a function of depth and photons will not be absorbed until deeper into the material. In order to absorb the majority of incident photons, the absorbing region should be made larger. However, if the diffusion length is small compared to the absorber, carriers will have a higher probability of recombining before being extracted. Thus, a careful tradeoff must be made in determining the optimum absorber length taking into consideration the expected operating temperature of the device. One way to expand the total absorber thickness while not running up against the limitations imposed by the diffusion length is to split the absorber among multiple stages in each of which, the carriers can be rapidly collected before recombining. In an ICIP, the total absorber length can be made large by increasing the number of stages while each stage's absorber can remain small enough so as not to exceed the diffusion length. This allows greater photon absorption and greater carrier collection. This presents an advantage for ICIPs operating in conditions or designed with

material for which the diffusion length is short. The diffusion length characterizes the probability that carriers will diffuse a certain length before recombining rather than setting a hard limit.

The diffusion length is dependent on both the diffusion coefficient and the carrier lifetime ($L_e = \sqrt{D_n \tau_n}$). The diffusion coefficient is further a function of temperature and the temperature-dependent mobility through the Einstein relation $D_n = (\frac{kT}{q})\mu_n(T)$. The first term of the product increases with temperature directly. The mobility, however, is the result of multiple processes and has a more complex temperature dependence.

The mobility directly relates the drift velocity, v_d, of a carrier to the electric field it experiences, E, by $v_d = \mu E$. The higher the mobility, the faster a carrier can move through a material within the presence of an electric field. The carrier's mobility can be impeded through interactions with phonons and impurities in the material. The mobility due to acoustic phonon scattering is approximated by $\mu_l \approx (m^*)^{-5/2} T^{-3/2}$ whereas the mobility due to ionized impurity scattering is approximated as $\mu_i \approx (m^*)^{-1/2} T^{3/2}/N_I$ where N_I is the ionized impurity concentration. One can see that the former decreases with temperature and the latter increases with temperature. Additional particle interactions can further complicate the mobility temperature dependence but generally, the overall mobility is a function of the individual mobilities through Matthiessen's rule given by[4]

$$\frac{1}{\mu} = \frac{1}{\mu_l} + \frac{1}{\mu_i} + ... + \frac{1}{\mu_{other}}. \tag{2.21}$$

and tends to have a peak at some low temperature (< 100 K) before decreasing with increasing temperature.[4] Since mobility tends to decrease with temperature, the diffusion length tends to decrease with temperature. This indicates that the advantages offered by the multiple stage ICIP architecture may be realized in high temperature IR detector applications.[10]

Another application in which the multi-stage approach may offer an advantage due to degraded diffusion length is in space-based infrared detectors. It has been shown that radiation-induced displacement damage in IR detectors decreases the carrier lifetime and the diffusion length.[11][12] This being the case, proving high operating temperature operation may provide some indication of a device's radiation tolerance at least in terms of quantum efficiency degradation. It would not, however, provide full insight into how the dark current would increase with radiation exposure. Typically with higher temperatures, the diffusion current increases more quickly than the G-R current whereas that may not be the case when increasing radiation induced defects.

In addition to the potential for high operating temperature and radiation tolerant applications, the ICIP architecture may off advantages where high speed detection is necessary. The speed of a device is in part dictated by the speed in which the detector's signal returns to zero once it ceases to be illuminated.[9] This means that any photogenerated electrons should be collected as quickly as possible. Its apparent that a high mobility will help in this regard. A shorter absorbing region will also increase the speed of the device as carriers have a shorter distance to travel before being collected. If a multi-stage device can mitigate the reduction in external quantum efficiency associated with a shorter absorber while offering other benefits such as low-noise, it would offer higher speed operation compared to a single-stage device.

From the above analysis, however, it is not readily apparent that a device with multiple smaller stages that needs to absorb an additional photon per stage should be expected to perform any better than a single stage device having an absorber small enough to avoid diffusion length limitations. To realize the advantage, one must also consider the additional impact the multiple stages have on the resistance, the dark current, and the noise.

For starters, each additional stage adds an additional set of barriers (one electron and one hole barrier) which can drive an increase in the device resistance. Keeping the total absorber thickness the same while increasing the number of stages it is split across has been shown to increase the resistance.[13] Comparing across detector sets with different numbers of stages, Lei et al showed that their 1000 μm square devices with 1, 4, 6, and 8-stage devices had $(R_0A)^{-1}$ values of about 60, 4.5, 2.5, and 1.5 $\Omega^{-1}cm^{-2}$ respectively clearly demonstrating the increased resistance caused by additional stages.[14] This increased resistance leads to lower Johnson noise as will further discussed and reduces pre-amplifier noise through higher impedance since any voltage noise will result in smaller fluctuations of current across the device.[14]

In addition to raising the resistance of the devices, the multi-stage architectures have been shown to have lower dark current.[13] It should be noted, however, that to the author's knowledge, a comparison between a single-stage device with a short absorber and a device with multiple of the same size absorber has not been made in terms of dark current. In fact, in theory, the multi-stage device dark current should represent the average dark current of the different stages.[9] This being the case, one would expect the dark current to be the same in the aforementioned potential comparison. The noise, however, may not be the same.

2.5.3 ICIP Noise

Considering now the noise in the multi-stage devices, Hinkey *et al.* have applied the Shockley-Ramo theorem to multi-stage devices of identical absorber thicknesses among stages to show that the dark current noise will be given by[10]

$$i_n^2 = 2q^2A\sum_{m=1}^{N_s}\beta_m^2(Y_m + R_m), \tag{2.22}$$

where A is the detector area, β_m is the percentage of the total device resistance

from the m^{th} stage, and Y_m and R_m are the collection and injection current densities in the m^{th} stage respectively. For the case with N_s identical stages, $Y_m = Y$ and $R_m = R$ and $\beta_m = 1/N_s$ such that the summation leads to

$$i_n^2 = \frac{2q^2A(Y+R)}{N_s} = \frac{2q^2I_{dark}}{N_s}, \tag{2.23}$$

showing that the noise current i_n will be reduced by $1/N_s^{1/2}$ compared to the shot noise of a single stage device. This does not account for Johnson or $1/f$ noise but indicates that if a device is shot-noise limited, the multi-stage architecture may reduce the noise below the single-stage limit.

In cases of a strong signal where the current is dominated by photocurrent, this may be a physically achievable advantage since photogenerated carriers would boost the current without the associated increase in Johnson noise or $1/f$ noise associated with G-R, surface or tunneling currents as discussed further in section 2.7.6.

The theoretical prediction that the shot-noise in multi-stage devices can be brought below that of a single-stage device has been applied in other architectures as well. The example most relevant to the ICIP structure is that of the four-zone quantum well infrared photodetector (QWIP). The basic band structure of the four-zone QWIP is shown in figure 2.3. The distinct "zones" in this architecture are similar the to regions of the ICIP and include an emission zone, a diffusion zone, a capture zone, and a tunneling zone.[15] Photons are absorbed in the emission zone, so named because of the emission of an electron from the quantum well into the quasi-continuum above the conduction band edge of the drift zone. The electrons then diffuse to the capture zone where they relax into a quantum well before tunneling through a barrier - the tunneling zone -into the next emission zone quantum well. The capture zone drives carrier transport much like the relaxation region in the ICIP. As in the ICIP, an additional photon must be absorbed in each stage.

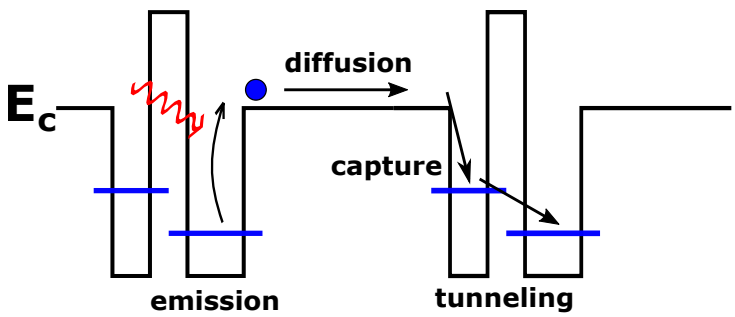

Figure 2.3: Stages of a four-zone QWIP which wherein the capture process drives transport and allows for photovoltaic operation.

Multiple theories have been presented on the noise gain in QWIPs.[16, 17, 18] In 1998, Schonbein et al, conducted direct measurements of n-type GaAs/AlAs/AlGaAs QWIPs and used the aforementioned theories to calculate the capture probability.[19] Applying the three theories to determine the quantum well capture probability from the measured noise and gain, they found that Beck's noise formulation agreed well with the anticipated probability of unity. In Beck's formulation, the QWIP noise gain is given by[17]

$$g_{n,QWIP} = \frac{I_n}{4qI_{dark}\Delta f} + \frac{1}{2N}, \tag{2.24}$$

where I_n represents the noise current in amps, and N is the number of stages. By measuring the noise at 1430 Hz, high enough where low frequency noise was expected to be negligible, Schonbein et al found a noise gain greater than or equal to 0.5 for a device with 20 stages which agrees very well with Beck's formulation in 2.24. This finding served not only to test the hypothesized noise gain theories surrounding QWIPs but was also a useful demonstration of the utility of noise measurements in determining gain more generally and for probing the mathematically derived theories surrounding the device physics. This work on ICIPs, in part, seeks to use noise measurements in a similar way to test the hypothesized noise gain theory in the literature.

2.5.4 ICIP Stage Current Matching

The above shot-noise analysis assumed identical stages in the multi-stage device. While this assumption is useful in the conception of noise reduction, it may not be desirable to have identical stages. It was mentioned previously that the absorption coefficient dictates the photogeneration rate at some depth in the material as given by 2.19. Integrating the photogeneration rate over an individual absorber thickness, d, will produce a smaller result deeper into the material ($\int_{d_1}^{d_1+d} g_{ph}(x)dx > \int_{d_2}^{d_2+d} g_{ph}(x)dx$ for $d_1 < d_2$). In order to make the currents in subsequent stages equal, the deeper stage must be larger so that the lower photogeneration rate is compensated by integrating over a larger distance. This is the rationale behind current-matched multi-junction solar cells where the first absorber is the shortest followed by increasingly thick absorbers.[20] A comparison has been made specifically between ICIPs with current-matched stages and non current-matched stages (equal absorber thicknesses).[21] Results showed that the current-matched ICIPs had responsivities about 1.5 to 2 times that of the non-matched devices at temperatures above 250 K. Interestingly, however, an electrical gain was observed in the non current-matched devices that increased the responsivity beyond what was expected.

Even though more carriers are generated in stages closer to the surface of incidence, the total current flowing through the devices must be conserved. Thus, even when the stages are not inherently current-matched and when zero external bias is applied, a forward bias will develop in the top stages due to hole accumulation and a reverse bias will develop in the deeper stages. The reverse bias in the deeper stages drives a thermal generation current in the same direction as the photogenerated current, thus inducing an apparent gain.[22] All of the devices in this work were designed to be current matched when illuminated by a blackbody spectrum but could not be considered current matched for shorter wavelength illumination. The consequences of this current mismatch are discussed further in the results where the ICIPs were

illuminated by a visible and SWIR laser.

2.5.5 ICIP Negative Differential Conductance

In addition to the phenomena described above, higher temperature IV curves of ICIPs have revealed regions of negative differential conductance (NDC) corresponding to a decrease in current with an increase in bias over a small bias range.[13, 22, 23] The number of NDC peaks in the IV curves have been consistent with the number of stages in the devices. This supports the theory that the NDC is due to resonant tunneling through the electron barrier which is made up of multiple quantum wells. Resonent tunneling through multiple quantum wells to create NDC has been used as the foundation for resonant tunneling diodes (RTDs), the theory of which can be used to help understand ICIPs. The same IV characteristics observed in the ICIPs have been observed and studied in RTDs explored for their use in building oscillators and terahertz switching devices.[24, 25, 26]

In a standard double barrier RTD, a quantum well is sandwiched between two heavily n-doped regions such that at equilibrium, its ground state energy is above the fermi level in the two adjacent regions. As the device is biased, the quantum well level aligns with the filled states in one n-type region (the emitter) above the conduction band and below the Fermi level. In the opposite n-type region (the collector), the Fermi level is pushed further down by the bias such that empty states above the Fermi level are in line with the quantum well ground state. This allows electrons to resonantly tunnel through the quantum well from the occupied states on one side of the double barrier to the vacant states on the other, causing an increase in current. As the device is further biased, the quantum well ground state eventually falls below the conduction band of the emitter and there are no longer occupied states able to provide electrons for the tunneling process. This causes a decrease in the current

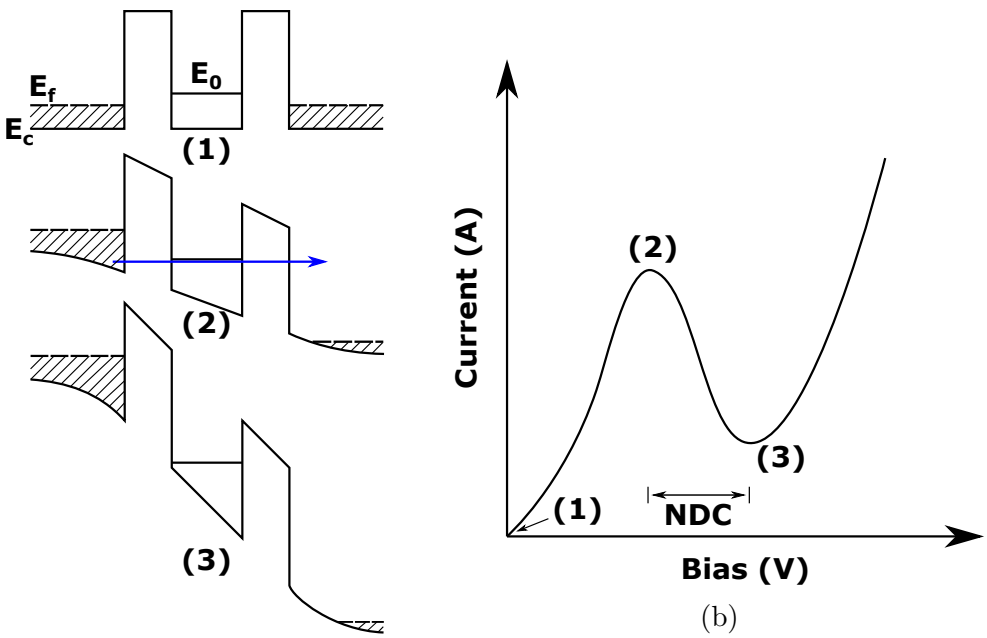

Figure 2.4: (a) Energy band diagrams of an RTD with increasing bias and (b) the resulting IV curve.

with increasing voltage leading to NDC. Figure 2.4 shows the three key bias regions described above for an RTD.

In the ICIPs, the electron barrier is made of multiple quantum wells. The NDC features in their IVs is theorized to result from a similar process as in the RTDs such that as the device is biased, the multiple quantum well ground energies align such that electrons in the hole barrier region can tunnel into the conduction band of the absorbing region in the next stage. Figure 2.5 shows the effect of biasing on an ICIP and the resulting resonant tunneling turn on. As the bias increases and, the quantum well states become unaligned again, leading to a drop in current and hence the NDC feature. It is suspected that resonant tunneling occurs through the barrier nearest the contact first followed sequentially by the other stages' barriers at increasing biases.[23] Changing the resonant tunneling feature in the IV provides an additional parameter for exploring the noise characteristics in ICIPs including the

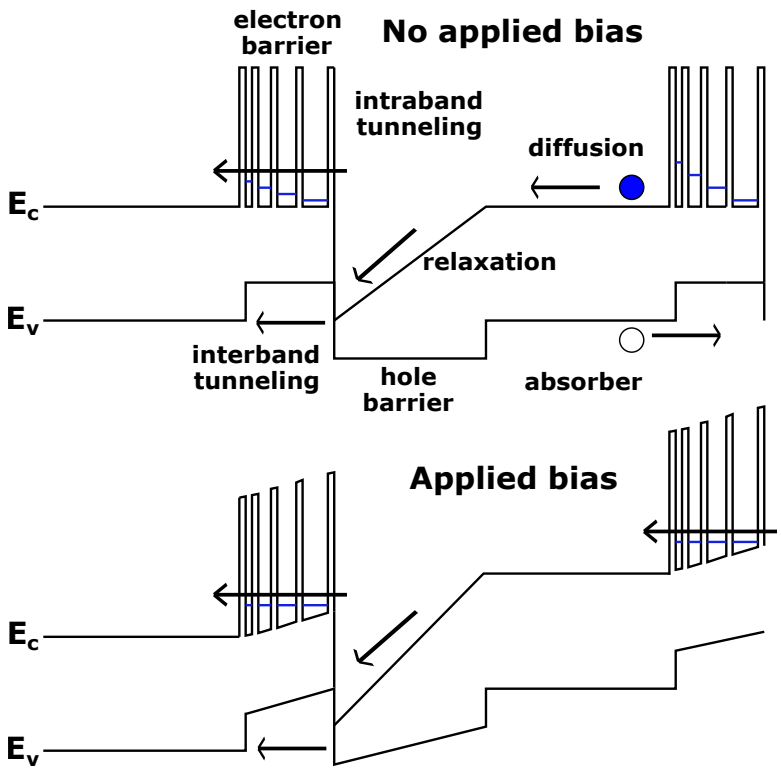

Figure 2.5: Multi-stage ICIP band diagram showing that increased external bias turns on resonant tunneling through the multi-quantum well electron barriers. The applied bias drops primarily over the barrier regions.

relationship between noise and tunneling processes and between noise and NDC.

2.5.6 Reported Performance

The ICIP structure has been used to create both MW and LWIR single element detectors and in some cases, full focal plane arrays.[27] They have been demonstrated using bulk material and superlattices as the absorbing layer. [13, 28] Additional work has been performed to suppress the intraband tunneling through the electron barrier by adding additional quantum wells, thereby lowering the dark current.[29, 30] When Johnson noise-limited performance is assumed, LWIR ICIPs operating at 300 K have been shown to have comparable or favorable D^* to HgCdTe photovoltaic devices with

similar cutoff wavelengths. [13]

2.6 Performance Metrics

IR detector performance is reported in multiple ways depending on the application. Three relatively universal ways of identifying the detector performance, however, are the cutoff wavelength, the quantum efficiency, and the dark current. The cutoff wavelength typically determines the application space in which the detector will be used. The quantum efficiency and dark current generally speak to how well the detector responds to incident light and how little unwanted current it produces respectively.

2.6.1 Cutoff Wavelength

The cutoff wavelength of a photon detector is dictated by the energy bandgap between the effective valence and conduction bands. In some cases, the energy difference between energy subbands dictates the cutoff or peak detection wavelength as with QWIPs. The cutoff wavelength is related to the bandgap by the relation $\lambda_c = hc/E_g$. For most semiconductors, the bandgap is a further a function of temperature given by[4]

$$E_g(T) = E_g(0) - \frac{\alpha T^2}{T + \beta}, \tag{2.25}$$

where α and β are material-specific constants on the order of 10^{-4} eV/K and 10^2 K respectively.[4] From the two relations above, it is apparent that the cutoff wavelengths of most IR detectors are expected to increase with temperature as the bandgap narrows. This is not true for HgCdTe detectors with high HgTe composition

for which the cutoff wavelength increases with temperature due to the semi-metal nature of the composition.[31]

The cutoff wavelength is determined by one of several conventions. One is to find the inflection point of the spectral response, another is to find the value at which the response falls to 50% of its maximum or other predefined value. In this work, cutoff wavelengths are reported using the former convention unless otherwise noted.

2.6.2 Quantum Efficiency

The efficiency with which an IR detector converts an incident photon into a collected electron contributing to the current is the quantum efficiency (QE). The external QE takes into account all photons incident on the detector and includes any losses due to reflection and recombination. The internal QE considers only those photons that penetrate into the device. Normally in reference to IR detectors, the unqualified term QE refers to the external QE and this work will maintain that convention.

Another performance parameter related to the QE is the responsivity. The responsivity reports the signal output, S to the IR input in terms of current or voltage per watt of incident power. The responsivity, $\Re$, is computed simply as[5]

$$\Re = \frac{S}{EA_d}, \tag{2.26}$$

where E is the incidence in watts per area, and A_d is the area of the detector.

2.6.3 Dark Current

Multiple current mechanisms were explained in section 2.3. All can contribute in different proportions to the overall dark current of an IR detector, the current produced by everything except photo generation. Dark current typically increases with

increasing temperature due both to a narrowing of the bandgap, making thermal excitation more likely since n_i is a strong function of temperature, and due to a shortened recombination lifetime. Devices designed for longer wavelength applications will typically have higher dark current for the same reasons. Thus, comparing the dark current of different devices is most useful when taking into account both the cutoff wavelength and the operating temperature of the device. This idea was formalized in the work by Tennant *et al.* in a 2007 by fitting the dark current density of state-of-the-art MCT detectors developed at Teledyne Imaging Systems which resulted in the formulation of "Rule 07" given by

$$J = J_0 e^{C(1.24q/k\lambda_c T)}, \tag{2.27}$$

$$\lambda_e = \lambda_c \; for \lambda_c \geq \lambda_{threshdold} \tag{2.28}$$

$$= \lambda_c / [1 - (\frac{\lambda_{scale}}{\lambda_c} - \frac{\lambda_{scale}}{\lambda_{threshold}})^{Pwr}] \; for \; \lambda_c < \lambda_{threshold}, \tag{2.29}$$

where $J_0 = 8367$, $Pwr = 0.5441$, $C = -1.163$, $\lambda_{scale} = 0.2008$, and $\lambda_{threshold} = 4.6351$.[32] Rule 07 is a commonly used metric for reporting the dark current of IR detectors (i.e. some multiple of Rule 07 for a device with a given cutoff and operating temperature). It doesn't provide any indication, however, of the QE of the device so must be used in the context of other performance parameters. In the development of the metric, a QE of 90% or greater was assumed.[32] This means that Rule 07 results for devices with lower QEs must be used with appropriate caution.

2.6.4 Noise

Noise concerns the temporal variation of what would ideally be a steady signal from an IR detector. In focal planes arrays (FPAs) and single element detectors, the noise

- together with the quantum efficiency and dark current - are used to determine the performance of the device. Noise limits the detectivity, the signal-to-noise ratio (SNR), and Noise Equivalent Temperature Difference (NEDT) which all hinder a user's ability to detect targets or accurately read the temperature variation across a scene.[2] Low-frequency noise can also cause pixel blinking that can lead to false target detections and can necessitate more frequent system calibration.

Noise is represented as the root-mean-square (rms) of the deviation of a signal from its mean or true value. For IR detectors, this measure is in current or voltage. It is apparent that if the rms of the baseline current or voltage exceeds the signal, the signal will not be discernible. Thus, the quotient of the signal and noise, known as the signal-to-noise ratio must be greater than one for adequate detection. A measure of the incident power needed to reach an SNR = 1 is called the Noise Equivalent Power (NEP) given by[2]

$$NEP = \frac{N}{\Re} \tag{2.30}$$

where N is the noise value in either volts or amps depending on the units of the responsivity used such that the NEP has units of watts. Knowing the NEP of a detector can be useful to determine the SNR if the incident power is known.

Similar in function to the NEP metric, the noise equivalent difference in temperature (NEDT) indicates the temperature difference in an observed object needed to cause a signal change greater than the value of the noise. For IR detectors used as thermal imagers, the NEDT conveys the temperature resolution of the detector.

The NEP and NEDT are useful for determining the limitations of a given IR detector but are not well-suited for comparing different detectors. Since the signal is dictated in large part by the number of photons incident upon the detector, the SNR varies with both incidence and device area making it a poor metric for comparing

different devices under different circumstances. The specific detectivity metric was developed due to these limitations and provides a method of describing an IR detector's signal to noise ratio normalized to the incidence, device area, and frequency bandwidth of operation. It is calculated as[2]

$$D^* = \frac{\Re\sqrt{A_d}}{N/\sqrt{\Delta f}}, \tag{2.31}$$

where N is the noise value in either volts or amps and Δf is the bandwidth. Together, the terms in the denominator give the noise spectral density in $A/\sqrt{Hz}$ or $V/\sqrt{Hz}$.

The above metrics can be applied to single element detectors as well as individual detectors in an array. To present the noise performance of an FPA, one or more of the above metrics is presented in the form of a histogram showing how many array elements exhibit a certain level of noise (NEP, NEDT, etc.). The mean, median, standard deviation, and extent of the distribution tail all provide useful metrics for the noise performance of an FPA.

The median of the distribution provide an idea of the overall noise that one expects to see across the FPA. In this case a lower median noise is better. The variance of the distribution provides an idea of how close most pixels are to exhibiting the median noise. A small variance is preferred and is one measure of the uniformity of an array. The third feature of the histogram, the tail, provides a measure of how many outlier pixels there are that exhibit a large amount of excess noise compared to the mean. Pixels in the tail of the distribution can be especially problematic since they may exhibit enough noise that even the upper limits of radiance from an application target will not be enough to surpass unity SNR.

Thus far, the noise has been discussed in terms of the rms value, a single measure of the amount of deviation in a signal. The rms value does not indicate the frequency with which the signal fluctuates. To provide a more complete picture of the noise in

a detector, it is useful to directly measure the noise power spectral density (PSD) as a function of frequency. The PSD provides the frequency-dependent rms voltage or current normalized to a 1 Hz bandwidth. Sometimes referred to as just the "noise spectrum," the PSD can reveal both general trends of noise with frequency or peak frequencies at which greater fluctuations in the signal occur.

Sources of noise and causes of different frequency dependencies will be discussed further in 2.7. Here, methods of characterizing the frequency dependence are presented. Two metrics used to summarize a PSD are the 3-dB frequency and the corner frequency. Typically, PSD spectra will exhibit higher low-frequency noise that tapers off to some nearly constant value, white noise, at higher frequencies. The 3-dB frequency is the frequency below which the noise is 3-dB greater than the white noise. The corner frequency on the other hand is determined by approximating the low and high frequency noise spectral portions with straight lines on a log-log plot and then recording the intersection of the lines.[2] This method is demonstrated in figure 2.6 using artificial noise data. The corner frequency is of less utility when the low and high frequency portions are not particularly linear. For both the 3-dB and corner frequency metrics, a lower value is desired. Additional methods of characterizing the low-frequency portion of the PSD were developed concurrently with experimental noise measurements on a variety of devices and will be discussed in the following sections.

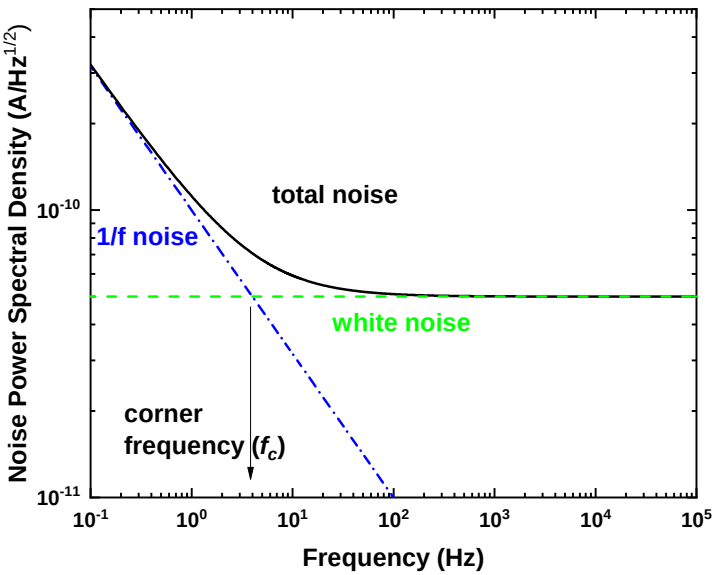

Figure 2.6: Artificial noise data illustrating the corner frequency noise performance metric.

2.7 Noise Sources and Physical Origins

Multiple sources of noise are present in IR detectors and the electronics necessary to read out their signal. Here, a review of the two white noise mechanisms is presented (shot noise and Johnson noise) along with a discussion of the current theories regarding the causes of frequency-dependent noise.

2.7.1 Shot Noise

The simplest form of noise is shot noise. Shot noise is the result of the discreet nature of charge. Electrons flowing through any substance will not uniformly arrive at the contact point. Their arrival times are dictated by Poisson statistics. As such, for any magnitude of current, there will be an inherent noise due to the random arrival

of electrons. The formula for shot noise current is given by

$$i_{N,S} = \sqrt{2qI}, \tag{2.32}$$

where I is the magnitude of current through the device. As such, IR detectors with low dark current are desirable for minimizing the shot noise.

Shot noise is typically one of smallest noise sources in a detector depending on the device resistance and overall current (when its contending with Johnson noise). There are cases, however, in which the noise can be reduced below the shot noise. In QWIPs and in ICIPs, some claim that the wells or stages provide additional sampling of the current. As in an experiment, the greater number of samples of a population, the lower the uncertainty in the determination of the behavior of the whole population. In an analysis mathematically analogous to increasing sampling, increasing the number of wells or stages in a device is claimed to decrease the noise by a factor of the square root of additional wells/stages.[10, 17]

2.7.2 Johnson Noise

An additional cause of noise is the thermal fluctuation of a device that causes a related fluctuation in the device's resistance.[33] The change in resistance manifests itself in the case of IR detectors as a current or voltage noise. The magnitude of the fluctuation in the current is proportional to the device temperature and inversely proportional to the square root of its resistance. Fully, the Johnson noise current in units of $\mathrm{A}/\sqrt{\mathrm{Hz}}$ is given by

$$i_{N,J} = \sqrt{4k_B T/R_d}, \tag{2.33}$$

where k_B is Boltzmann's constant, T is the device temperature, and R_d is the differential resistance (dV/dI) of the device which can be calculated from the IV curve.

As can be seen from equation 2.33, devices with larger resistance values are desirable to minimize Johnson noise.

2.7.3 Noise Estimation

Uncorrelated noise sources add in quadrature such that the total noise current for n uncorrelated sources is given by

$$i_{N,tot}^2 = i_{N,1}^2 + i_{N,2}^2 ... i_{N,n}^2. \tag{2.34}$$

At this point in the discussion, the two noise sources of a device most easily estimated have been covered. Shot noise and Johnson noise are uncorrelated noise sources so the total noise current due to both is given by

$$i_{N,T} = \sqrt{2qI + 4k_B T/R_d}. \tag{2.35}$$

As mentioned above, in ICIPs, additional stages theoretically reduce the shot noise by a factor of the square root of the number of stages.[28] If this is the case, the ICIP white noise could be given by

$$i_{N,ICIP} = \sqrt{2qI/N_S + 4k_B T/R_d}, \tag{2.36}$$

where N_S is the number of device stages. The noise of many ICIP devices in the literature, however, was assumed to be Johnson noise limited so that the additional stages do not reduce the noise except through increasing the differential resistance.[13, 21, 30, 34, 35]

2.7.4 Bias-induced Noise

When an external bias is applied to a detector, the voltage noise of the source $v_{N,vs}$ will induce a current noise in the detector through Ohm's law such that [36]

$$i_{N,vs} = v_{N,vs}\frac{dI}{dV}_{det}. \tag{2.37}$$

This is separate from the differential resistance-dependent Johnson noise of the detector. In order for the bias-induced noise to represent an appreciable component of the overall noise, $v_{N,vs}$ must be on the order of $\sqrt{4k_BTR_{diff}}$ which implies that as the temperature and the device differential resistance increase, the bias-induced noise will represent a diminishing portion of the total noise that would be measured in the external circuit.

2.7.5 Random Telegraph Signal Noise

Random Telegraph Signal (RTS) noise is characterized by the hopping of a signal between 2 or more relatively discreet states. Much work has been done to distinguish RTS from other types of noise both in its identification and to describe its physical cause.

It is apparent from the literature that certain material and device systems are more prone to exhibit RTS noise over others. HgCdTe is known as a high performance material (high QE and low dark current) across a large range of wavelength applications from around 1 μm in the SWIR to 30 μm in the VLWIR.[37] Compared to III-V group based semiconductors, however, HgCdTe may have lower uniformity and wandering "blinker" array elements due to RTS noise.[38] These blinking elements can give the false indication of target detection for applications in which a target may occupy only a single array element.

2.7.6 1/f Noise

As mentioned in section 2.6.4, the noise spectra of IR detectors often exhibit higher magnitudes at lower frequencies. The excess noise at low frequencies is typically referred to as $1/f$ noise.[39] $1/f$ is refers to noise spectra with frequency dependence of the form $1/f^{\alpha}$ with α varying between about 0.5 and 1.5. Of key note is that $1/f$ refers to the common frequency dependence of the noise power such that the voltage noise squared is proportional to the inverse frequency ($v_n^2 \propto 1/f$) whereas the voltage noise commonly measured in $\mathrm{V}/\sqrt{\mathrm{Hz}}$ will actually show a $1/f^{1/2}$ frequency dependence.[2] This implies also that current noise measured in $\mathrm{A}/\sqrt{\mathrm{Hz}}$ found by dividing the voltage noise by the feedback resistor (or trans-impedance gain) of an amplifier will yield a spectrum where $i_n \propto 1/f^{1/2}$ for true $1/f$ noise.

A large body of work exists presenting different experiments and physical theories involving $1/f$ noise in a variety of semiconductor devices. Noise spectra of HgCdTe photodiodes were found to exhibit $1/f$ noise linearly proportional to the surface generation current, I_s through the relation

$$i_N = \alpha I_s f^{-1/2}, \tag{2.38}$$

where α was a fitting parameter found to be $\approx 1 \times 10^{-3}$ in the work by Tobin et al in 1980.[40] Since then the coefficient, α, has been referred to by some as the Tobin coefficient for summarizing the noise performance. In a more generalized form, the Tobin coefficient is found using the noise value at 1 Hz so that $\alpha = i_N(1\mathrm{Hz})/I$ where I is the device current. This allows the Tobin coefficient to be reported even when the exact frequency dependence is not $1/f^{1/2}$ as in equation 2.38.

$1/f$ noise has also been linked to the tunneling current, I_t, in reverse-biased HgCdTe photodiodes operating over temperatures and biases where trap assisted

tunneling dominated the current through the relation

$$i_N = \alpha I_t^{\beta} f^{-1/2}, \tag{2.39}$$

where α and β were fitting parameters found to be $\approx 1\times10^{-6}$ and ≈ 0.5 respectively.[41]

In HgCdTe Metal-Insulator-Semiconductor (MIS) IR detectors operating below 65 K, $1/f$ noise was related to a combination of minority carrier generation in the depletion region and band-to-band tunneling while in the same devices operating above 90 K, the $1/f$ noise was attributed to HgCdTe-ZnS interface states.[42]

Chapter 3

Methodology

3.1 Device Information

The devices tested in this work were selected to represent different device architectures in order to provide insight into the relationship between different current mechanisms and noise. The first detector type was a III-V nBn detector with a superlattice absorber. The second detector type included a set of ICIPs with 1, 4, 6, and 8 stages with superlattice absorbers. All of the detector types consisted of one or more process evaluation chips (PECs). The nBn and ICIP PECs were processed using different masks but each contained a set of variable area square detectors with areas ranging from 50×50 μm^2 to 1000×1000 μm^2. All of the PECs were mounted in 64-pin leadless chip carriers (LCCs). Following is further information about the detectors.

The nBn device selected for test was a MWIR detector with an InAs/InAsSb superlattice absorbing layer. At 130 K, the cutoff wavelength was 5.3 μm. The quantum efficiency at a wavelength of 3.3 μm was 89% at 130 K and a reverse bias of 100 mV. At this bias and temperature condition, the device exhibited a dark

current density of 1.78 μA/cm^2 which is 7.5 times Rule 07. After radiometric and noise characterization, the device was radiated with 63 MeV protons at a fluence of $7.5 \,\mathrm{x}\, 10^{11}$ cm^{-2} (TID 100 kRad (Si)). After irradiation, the quantum efficiency dropped to 50% and the dark current density increased to 41.08 μA/cm^2 (59 times Rule 07). The radiation exposure of the nBn was opportunistic given other device radiation experiments within the research group and was used to explore the changes in the device QE, dark current, and noise following the introduction of additional material defects.

Four ICIP PECs were tested. The ICIP devices were each from a separate wafer. The processed but unpackaged devices were provided by a research team at the University of Oklahoma. The individual chips were then epoxied to LCCs and wire-bonded in-house. Devices from the same wafers were reported on previously detailing their growth, fabrication, and radiometric performance.[13] The four PECs included a single stage (S#3-1), a four-stage (S#3-4), a six-stage (S#3-6), and an eight-stage (S#3-8) ICIP architecture. The one and four stage devices had the same total absorber thickness of 1386 nm while the six and eight-stage devices had the same total absorber thickness of 2292 nm. The devices were designed with the intention of current matching such that deeper absorbers were thicker. The absorbing layers all consisted of the same 60 Å InAs/GaSb superlattice period. The electron and hole barriers were made up of three GaSb/AlSb QWs and seven InAs/Al(In)Sb QWs respectively. Lei et al reported the cutoffs of the devices at 200 K using the point at which the signal was 10% of its peak value which they called the 90% cutoff. For the one, four, six, and eight stage devices the cutoffs were found to be 9.1, 9.3, 9.0, and 8.8 μm respectively making all of them LWIR detectors.[13] LWIR detectors were chosen to more easily test the high-temperature advantages of the ICIP structure. The term "high-temperature" is somewhat relative to the cutoff of the devices. Since LWIR detectors have a smaller bandgap, they typically have a higher dark current at a specific temperature than MWIR and SWIR parts. Thus, one can reach the

limiting temperatures more easily if they are LWIR detectors.

3.2 Equipment

Multiple test systems were deployed to test the radiometric and noise performance of both the nBn and ICIP devices. Three separate liquid nitrogen-filled dewars were used with different combinations of internal cold shields, limiting apertures, and bandpass filters. Here, the multiple test apparatuses are explained in detail and related to the reasons for using each.

3.2.1 Small Blue Dewar

In order to measure the spectral response of the detectors, a dewar with a 5 inch diameter outer can was used referred to as the "Blue" dewar. Internally, the dewar contains a cold finger equipped with a 68 pin LCC socket resting at 2.36 inches from the pinhole when present. When using a pinhole of 0.2", the $f/\#$ of optical setup was about 12. The outer can window is two inches in diameter and made of ZnSe with a spectral pass range from about 0.5 to 20 μm. The Blue dewar has a removable inner cold shield equipped with a gravity-shuttered cavity that houses a pinhole and filter. For the spectral response measurements, the inner shield was fully removed so the device could be fully exposed to the source from a Fourier Transform Infrared Spectrometer (FTIR). The Blue dewar contains external ports to interface a bundled set of BNC cables, one each for selected pins on the internal LCC socket. For spectral measurements, output from the devices were connected to a Keithley 428 transimpedance amplifier (TIA) capable of both sourcing a bias voltage and converting the output device current to a measurable voltage with selectable gain ranging from 10^3 to 10^8 V/A. The output of the TIA was interfaced with a Nicolet FTIR.

Prior to each set of spectral response tests, the spectral response of an Eltec pyroelectric IR detector was tested to be used as the background measurement for the purposes of normalizing out absorption peaks due to atmosphere. The device spectral responses were measured in arbitrary units and divided by both the background and their own value at an arbitrarily defined wavelength for normalization. The cold finger has a temperature sensor/heating element package allowing the spectral response to be measured in this way for multiple biases and temperatures ranging from 77 K to about 320 K. The Blue dewar was also used for radiometric characterization of the ICIPs at all temperatures presented and for noise measurements on the ICIPs for temperatures above 130 K due to limitations in the "Noise dewar" further discussed below.

3.2.2 HiRad Dewar

The second dewar used had an 11-inch outer can and was equipped with two inner cold shields. This dewar contained two pour filled liquid nitrogen reservoirs, the innermost of which could be used to house liquid helium but was not used for that purpose in this work. The dewar is designed to contain mostly aluminum parts rather than stainless steel which can become radioactive after radiation exposure.[43] Thus, it is referred to as a High Radiation or "HiRad" Dewar. The innermost can also houses a gravity shuttered cavity for a pinhole and bandpass filter. The dewar contains a 68 pin LCC socket thermally mounted on top of a cold block as well as two temperature sensors and a heating element, allowing measurements to be taken at device temperatures ranging from nearly 4 K (with LHe) to about 320 K while the cold shields remain at liquid helium or nitrogen temperatures. The dewar has a two-inch external ZnSe window with a spectral pass range from near 0.5 to 20 μm. When present, the pinhole sits at 6.3 inches from the PEC. For a typical pinhole of 0.15" diameter used in the HiRad dewar, the dimensions give an $f/\#$ of approximately

42. The HiRad dewar contains external ports for bundled sets of coaxial cables. For dark current measurements, devices are connected directly to SMUs whereas with photocurrent measurements, they are connected first to an external TIA and then to a lock-in amplifier (LIA) which locks to the frequency of a blackbody-mounted chopper.

3.2.3 Noise Dewar

The third dewar used in device characterization is known as the "Noise dewar." While the first two dewars are designed for radiometric characterization including dark current and quantum efficiency, they are not optimized for low noise measurements. They both rely on external TIAs for conversion of the device current to a voltage and for gain. The Noise dewar is designed with a custom-built TIA wherein some of the key components are housed in the dewar close to the PEC and cooled to liquid nitrogen temperature in keeping with previous low-noise amplifier circuit designs for testing IR detectors.[45, 46] Figure 3.1 shows the circuit diagram of the Noise dewar setup. The source-follower MOSFET and feedback resistor are packaged together in a hybrid impedance converter (HIC). The HIC is wired to an internal circuit board connected to the LCC socket and each HIC sits within 3 inches from the PEC. This offers two advantages over the external TIA. First, the HICs are cooled to liquid nitrogen temperature inside the dewar and thus, the Johnson noise of the feedback resistor is $\sqrt{77/300} \approx 0.5$ times what it would be for a resistor at room temperature. The second advantage is that amplification of the device current and the device noise occurs inside the dewar very close to the actual device. Small vibrations and electrical pickup can generate noise in wires. By reducing the amount of wire between the device and the amplification stage, this minimizes the amplification of such noise.

The output voltage of the TIA can be used both to monitor the current of the

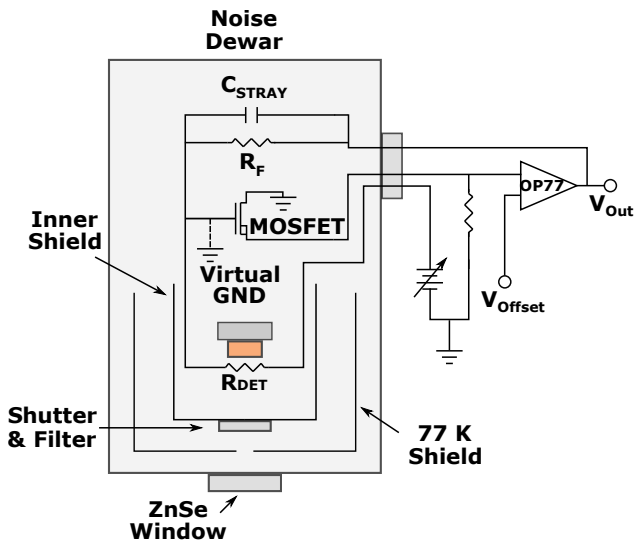

Figure 3.1: Diagram of the TIA with feedback resistor and MOSFET cooled in the cryostat. Virtual ground is established at the MOSFET gate such that (R_{Det}), V_{out}/R_f yields an equivalent current to that through the device.

device through the relation $I_{det} = V_{out}/R_{feedback}$ and the noise current of the device through the relation $i_{n,det} = v_{n,out}/R_{feedback}$. The op-amp was powered by a Hewlett Packard 6253A Dual DC power supply and a Keithley 236 SMU was used to bias the device under test (DUT). To measure the noise, V_{out} was connected to a SR770 Network Analyzer which internally collects time signal data and uses a Fourier transform to generate the PSD as a function of frequency. The Noise dewar TIA setup has been used in previous work measuring the noise of InAs/GaSb-based nBn MWIR detectors and was shown to have a baseline system noise more than one order of magnitude lower than the conventional, external TIA setup.[47]

The dynamic range is limited on the lower end by the SMU and on the higher end by the op-amp power supply. In order to minimize the feedack resistor Johnson noise, a large resistance value is desirable. However, too large of a feedback resistor would lead to saturation of the op-amp at the 15 V power supply voltage. Thus, the feedback resistor value is typically chosen to result in an output voltage of one volt at a specified bias and device operating temperature. The available feedack

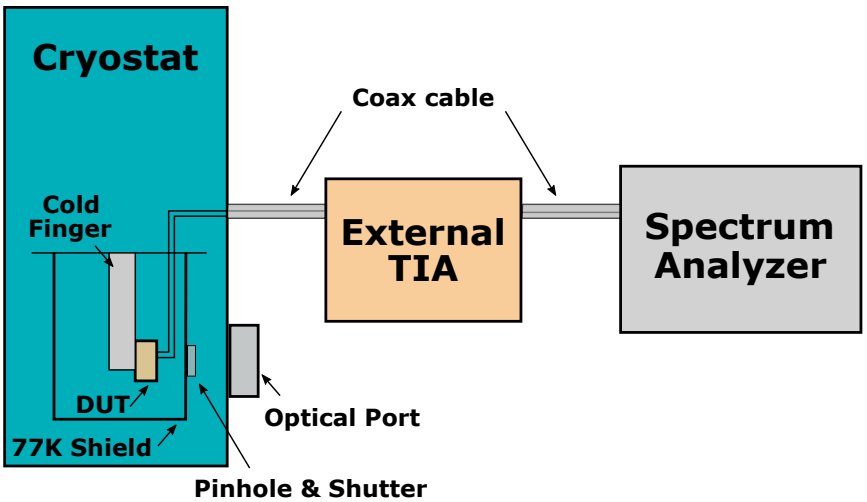

Figure 3.2: Diagram of the small blue dewar interfaced with the external TIA and Spectrum Analyzer for noise measurements.

resistor values ranged from 1.0×10^5 to 5.0×10^{12} Ω. In some circumstances, the device current was too high for even the smallest feedback resistor to be used without saturating the op-amp. In such circumstances, the current was high enough that the associated noise current was expected to dominate externally introduced noise from the external TIA system. For the ICIP devices operating at temperatures above 130 K, the blue dewar with an external TIA was used to measure the device noise through the setup shown in figure 3.2. The ability to measure the device noise was validated by comparing the PSDs obtained in the Noise dewar near the threshold 130 K operating temperature with those obtained from the Blue dewar.

Chapter 4

Results

4.1 nBn Characterization

The radiometric and noise characterization suites described above were first used to test the nBn detector with attributes described in section 3.1. The sections below describe the device characterization before and after irradiation by a 63 MeV proton source.

4.1.1 Pre-irradiation Radiometric Characterization

The radiometric and noise characterization of the nBn PEC described in chapter 3 was reported on previously by the author.[48] Characterization took place in multiple phases. First, it was loaded in the Blue dewar for spectral characterization using the methods described in section 3.2. The spectral response was collected at 130 K at a reverse bias of 60 mV. Figure 4.1 shows the normalized spectral response in arbitrary units. The cutoff wavelength found using the inflection point spectrum was found to be 5.5 μm. In order to test the dark current and calibrated photocurrent, the PEC

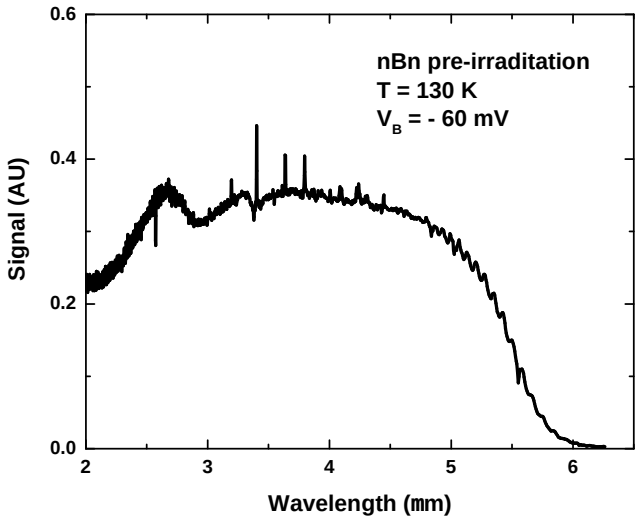

Figure 4.1: Pre-irradiation spectral response of the nBn at 130 and a reverse bias of -60 mV.

was then loaded into the HiRad dewar. A spectral bandpass filter ranging from 3.1 to 3.5 μm and a pinhole of 4.064 mm were loaded into the innermost cold shield of the dewar.

In the HiRad dewar, the dark current density vs bias (IV) curves were collected from a bias of -800 to 200 mV at 130 K. The IVs are shown for devices of multiple sizes in figure 4.2. From the figure, it is apparent that the smaller devices have a higher dark current density which is an indication of either lateral diffusion from around the nominal mesas and/or surface current. The current for all of the devices is relatively flat across the voltage range from -0.1 to -0.6 V. A small slop is observed, however, indicating that the diffusion and G-R current components are comparable. In higher reverse bias the current rapidly increases likely due to tunneling. Later Arrhenius analysis shown below confirms these indications.

To determine the photocurrent and QE of the devices, the internal shutter was opened and a blackbody at 900 K was placed at the external window of the de-

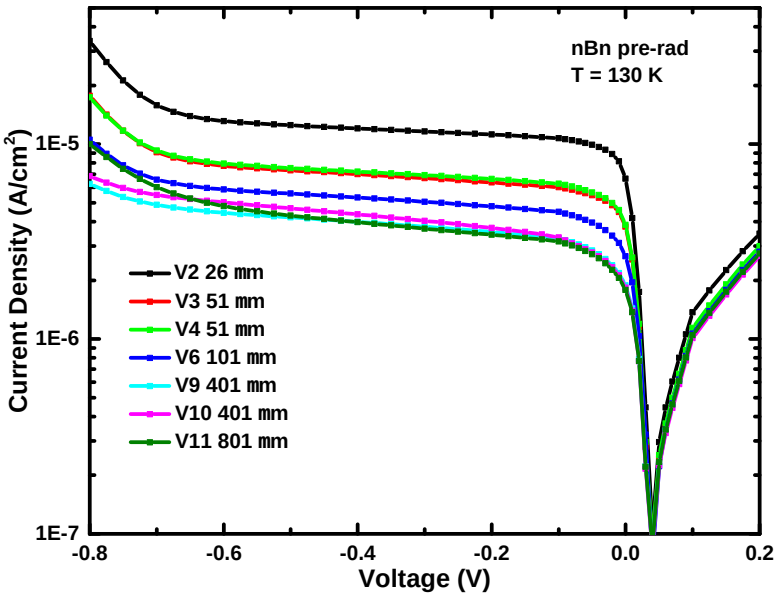

Figure 4.2: Dark current density curves for different sized devices at 130 K.

war such that the PEC would be flood illuminated through the pinhole. Using a chopper at a frequency near 10 Hz, the calculated irradiance on the devices was 2.4×10^{14} photons/cm^{2}s. The resulting photocurrent as a function of bias (PIV) curves are shown in figure 4.3.

In order to determine the QE, the photocurrent value of a specific bias was collected repeatedly (18 times) per device to generate an uncertainty in the measurement. Assuming that the photocurrent follows the form

$$I_{ph} = q\eta E_q A_{dev}, \tag{4.1}$$

where E_q is the irradiance and A_{dev} is the device area, the QE (η) can be determined by fitting a plot of the photocurrent vs device length. For a square mesa that is shallow etched, $A_{dev} = (L + 2L_{OC})^2$ where L is the nominal mesa length and L_{OC} is some length beyond the defined mesa from which carriers can still be collected, also

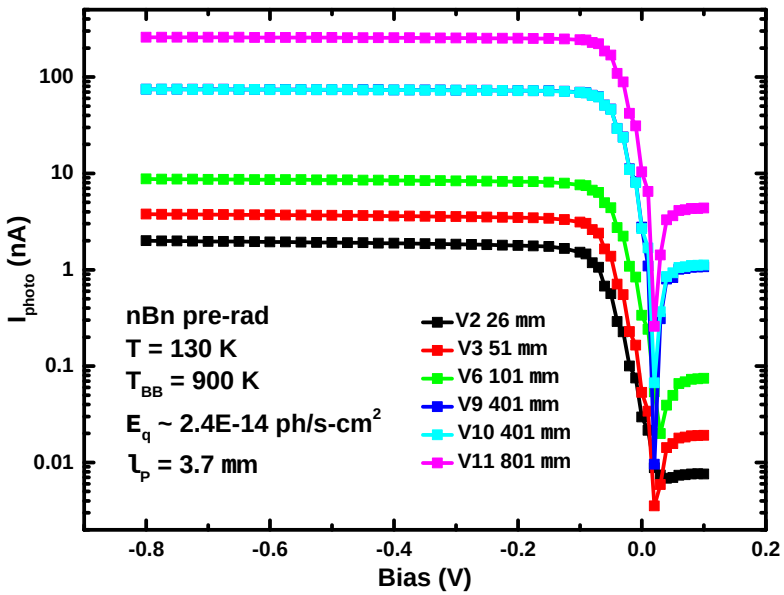

Figure 4.3: Photocurrent curves for different sized devices at 130 K.

known as the optical collection length. Thus, equation 4.1 can be re-written as

$$\sqrt{I_{ph}} = \sqrt{q\eta E_q}L + 2\sqrt{q\eta E_q}L_{OC}, \tag{4.2}$$

This is just the formula of a line where $\sqrt{I_{ph}}$ is a function of L, the slope $m = \sqrt{q\eta E_q}$ and the constant $b = 2\sqrt{q\eta E_q}L_{OC}$. Figure 4.4 shows the square root of the photocurrent plotted vs mesa length. Fitting a line to the data and using $L_{OC} = b/2m$ yielded an optical collection length of 22.7 μm. Using $\eta = m^2/qE_q$ yielded a QE of 90%.

After the photocurrent was collected and QE calculations complete, the device was cooled to 80 K and the dewar shutter was closed to start a sweep of IV curves vs temperature. IV curves were collected at temperatures from 80 to 220 K with 14 total temperature values approximately evenly spaced in $1/T$ space for an Arrhenius analysis. Figure 4.5 shows the resulting dark current density curves for the different temperatures. It is apparent from the curves that the devices were tunneling-limited

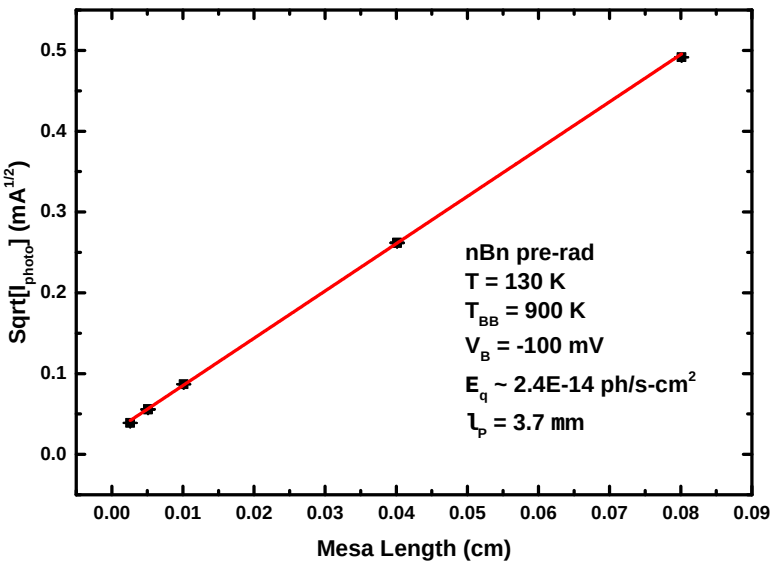

Figure 4.4: Photocurrent vs mesa length fit for determining quantum efficiency at optical collection length.

at high reverse bias ($>$ 700 mV) at temperatures below about 147 K. In order to more precisely determine the dominant current mechanism at different biases, the activation energy was sought using an Arrhenius analysis. Figure 4.6 shows the dark current at -100 mV for a 51 μm device as a function of $1/k_BT$. From the slope of this plot, an activation energy of $\approx$ 215 meV was found at temperatures above 147 K which is close to the bandgap of the material and indicates diffusion-limited current. Below 147 K, the device appeared G-R limited in the bias range from -200 mV and -600 mV. The very shallow temperature dependence of the current at -800 mV shown in 4.6 confirmed that the current was tunneling limited.

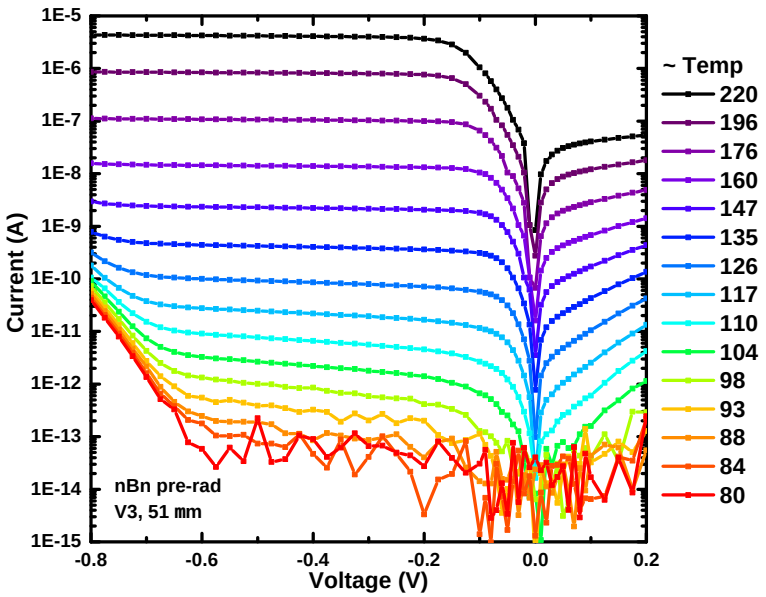

Figure 4.5: IVs taken in the HiRad dewar for a 51 μm square device at temperatures from 80 to 220 K.

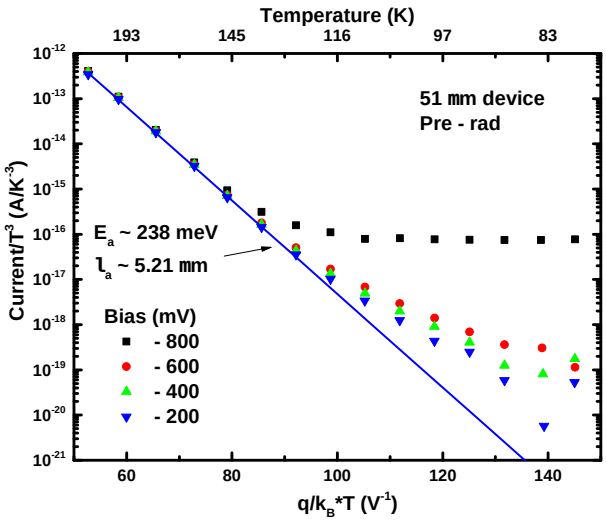

Figure 4.6: Arrhenius plot of a 51 μm device indicating diffusion limited dark current above 140 K between -200 mV and -600 mV, G-R limited between -200 mV and -600 mV for lower temperatures, and tunneling limited at -800 mV.

4.1.2 Post-irradiation Radiometric Characterization

After characterization of the radiometric performance and the noise characteristics, the nBn PEC was subjected to a single dose of 63 MeV protons to a fluence of 7.5×10^{11} cm^{-2}. The PEC was uncooled and not biased during irradiation. The nBn device shown here is similar in material structure to the family of detectors presented in reference [12] where it was explained that the Bragg peak of the 63 MeV protons was calculated to appear far past the active region of the device. Thus, the energy deposition and defect generation were expected to be nearly uniform as a function of depth within the chip.

Typically, in-situ step dosing is preferred while the device is held at a constant temperature. For the nBn structure presented here, however, that was not possible and was not deemed necessary to reach the end goal of comparing the noise current pre- and post-irradiation. For illustration of the step dosing change in dark current, however, Fig. 4.7 shows the change in the dark current of an nBn T2SLS MWIR detector from the same research program exposed step-wise up to a proton fluence of 7.5×10^{11} cm^{-2}. The dark current magnitude and slope in reverse bias typically both increase with increasing proton dose. This is the result of increasing defects in the detector which increases both the diffusion current and generation current.[12]

The dark current density curves of the subject nBn device post-irradiation are shown in figure 4.8. As expected, the magnitude and slope of the curves in reverse bias increased across devices. In order to verify the change in activation energy, and hence, the dominant current sources, the IV curves were collected again as a function of temperature and are shown in figure 4.9. The dark current was extracted at -100 mV and plotted as a function of $1/k_BT$ in figure 4.10. Comparing this with figure 4.6 shows an increase in G-R current up to 180 K compared to pre-irradiation and an increased tunneling current at -600 mV for temperates below about 90 K. For

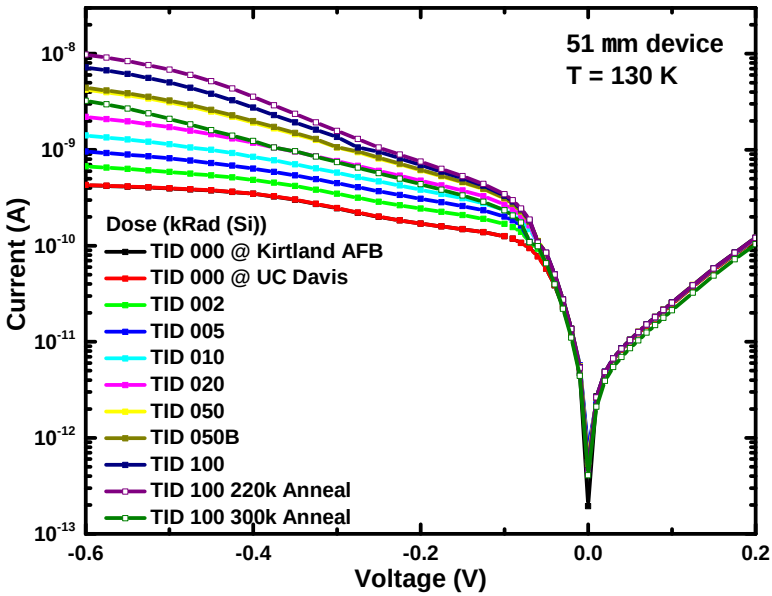

Figure 4.7: Illustration of the increase in dark current as a function of 63 MeV proton dose for a T2SLS nBn MWIR device similar to that studied in this work to a total fluence of 7.5×10^{11} cm^{-2}.

a bias of −800 mV, the dominance of tunneling current is even more distinct below about 100 K as indicated by the lack of current dependence on temperature.

The QE and L_{OC} were calculated after irradiation and the resulting values were 50% and 5.6 μm respectively. This represents a decrease of about 45% of the original 90% QE and a 75% reduction in the L_{OC} from the pre-rad value of 22.7 μm.

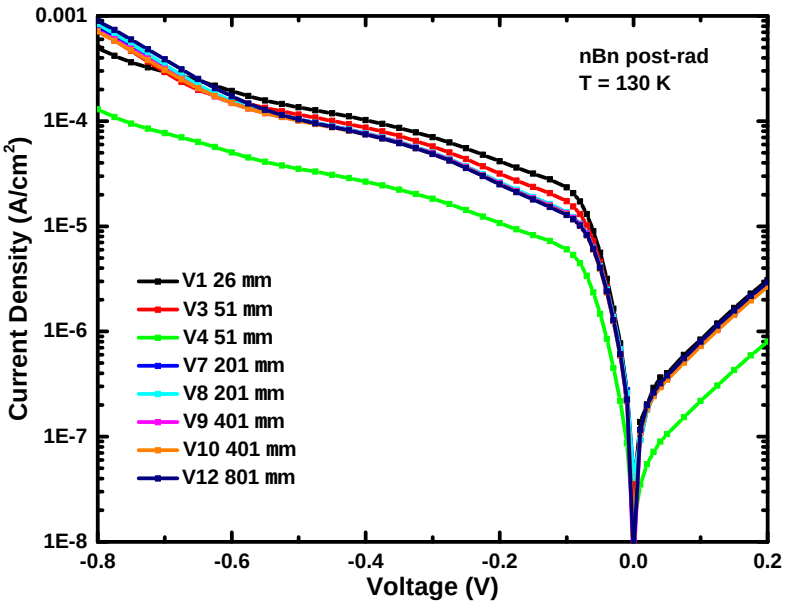

Figure 4.8: Post-irradiation dark current density curves for different sized devices at 130 K.

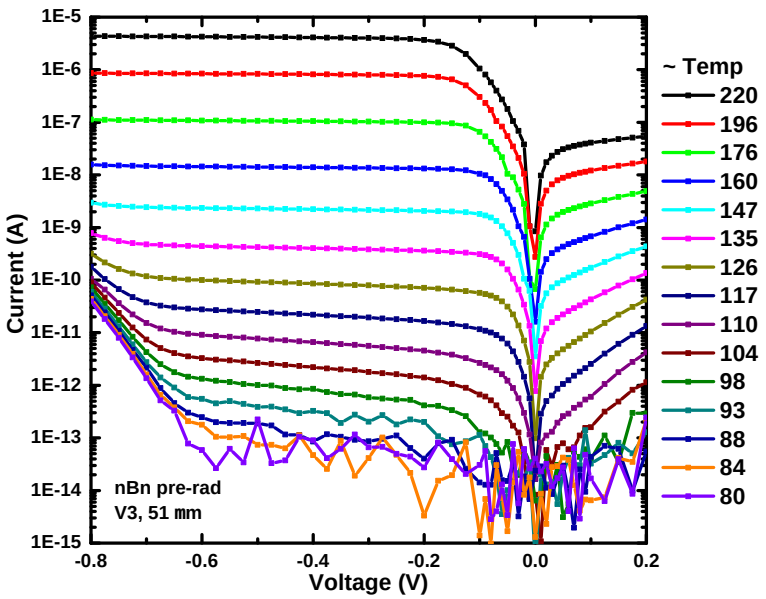

Figure 4.9: Post-irradiation IVs taken in the HiRad dewar for a 51 μm square device at temperatures from 80 to 220 K.

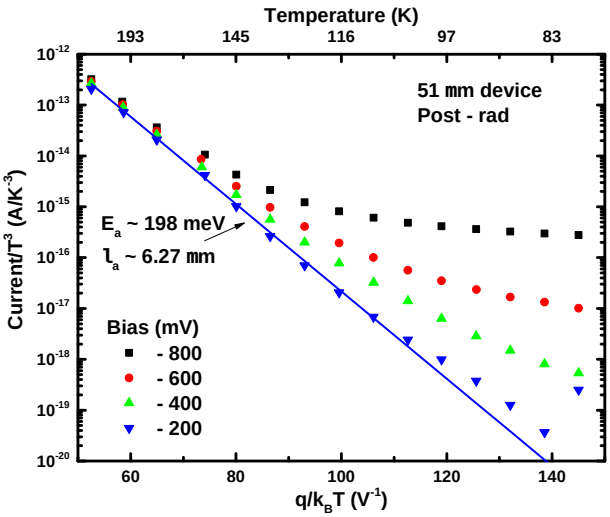

Figure 4.10: Post-irradiation Arrhenius plot of a 51 μm device indicating an increase in G-R current up to 180 K compared to pre-irradiation and an increased tunneling current at -600 mV for temperatues below about 90 K. For a bias of -800 mV, the dominance of tunneling current is more distinct below about 100 K.

4.1.3 Noise Estimation and Detectivity

Using the values for QE and dark current obtained above, the detectivity of the devices can be computed using the conventional approach described in section 2.6.4 with equation 2.35 assuming the detector is limited by shot and Johnson noise only. In order to do this, the quantum efficiency must be converted into a responsivity value through the relation

$$\Re(\lambda) = q\eta(\lambda)\frac{\lambda}{hc}. \tag{4.3}$$

Equation 4.3 yields pre and post-rad responsivities at 3.3 μm of 239.4 A/W and 133.0 A/W respectively. At 130 K and a bias of -200 mV, the current noise pre and post-irradiation of the 200 μm device was calculated using 2.35 to be 2.06×10^{-14} A/$\sqrt{\text{Hz}}$ and 6.23×10^{-14} A/$\sqrt{\text{Hz}}$. Using these noise values to calculate the D^* gives a pre and post-irradiation estimation of 2.32×10^{14} cm$\sqrt{\text{Hz}}$/W and $4.27 \times$

10^{13} cm$\sqrt{\text{Hz}}$/W. It is clear even from using the estimated noise value post-irradiation that the exposure caused significant performance degradation. To further explore the whether actual device noise was affected by the radiation, noise spectra were collected pre and post-irradiation. The results of both are discussed in the following section.

4.1.4 Noise Power Spectral Density

The Arrhenius analysis results showed that under different bias and temperature conditions, different current mechanisms dominated the overall current of the nBn device. The introduction of defects through proton irradiation increased both the G-R and tunneling currents. In order to investigate the relationship between current types and noise, noise spectra were collected at different temperature and bias regimes pre-irradiation and again post-irradiation.

The simplest experiment was conducted first in which the device temperature was held constant at 130 K while the bias was changed in increments of 200 mV from 200 mV forward bias to 800 mV reverse bias. Figure 4.11 shows the resulting PSDs. The results showed that for reverse biases of 200 to 600 mV, the measured noise was very close to the estimated noise over the frequency range 0.1 to 100 Hz. At higher frequencies, all of the spectra are seen to roll off likely due to the bandwidth of the circuit given by $1/\sqrt{(RC)}$. Notably, the agreement is greatest for biases shown to be most diffusion limited (-200 and -400 mV). At -600 mV, the low frequency noise started to exceed the prediction by a larger factor. At -800 mV, where the device was shown to be tunneling limited, the PSD shows no agreement with calculation, with low frequency noise as much as 7 times greater. The -800 mV spectrum shows a clear frequency dependence that most closely resembles $1/f^{1/4}$ up to 100 Hz. This measurement gave clear indication that the noise PSD shape was influenced by the dominant current mechanism.

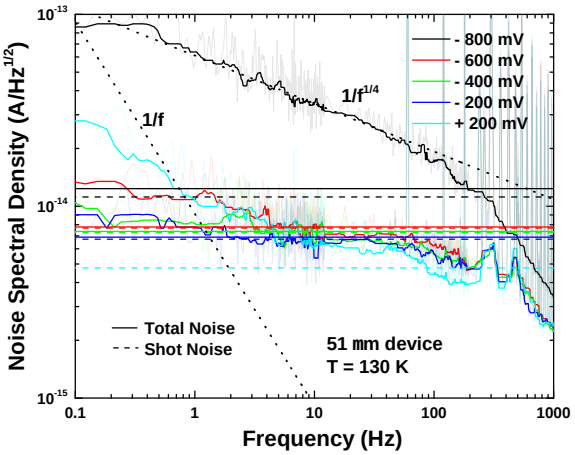

Figure 4.11: Noise PSD for a 51 μm nBn device at 130 K using a feedback resistor of 1 GΩ. The calculated shot and total noise are shown as dashed and solid horizontal lines respectively. $1/f$ and $1/f^{1/4}$ slope lines are included for illustration.

The measurements were repeated at a temperature of 117 K and the results shown in figure 4.12 with the same trend; noise currents matched equation 2.35 well where the current was diffusion limited but showed a $1/f^{1/4}$ dependence at high reverse bias where the current was again tunneling limited.

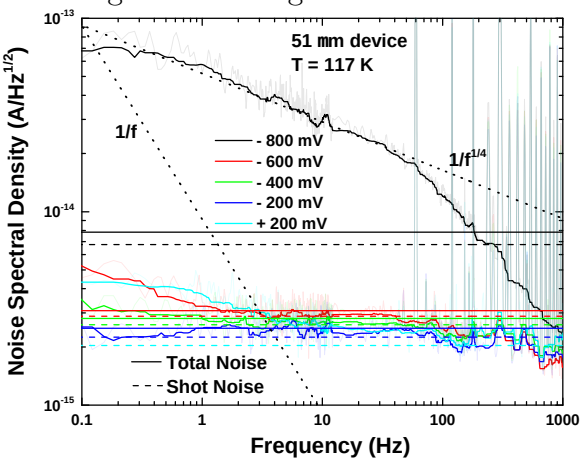

Figure 4.12: Noise PSD for a 51 μm nBn device at 117 K using a feedback resistor of 1 GΩ. The calculated shot and total noise are shown as dashed and solid horizontal lines respectively. $1/f$ and $1/f^{1/4}$ slope lines are included for illustration.

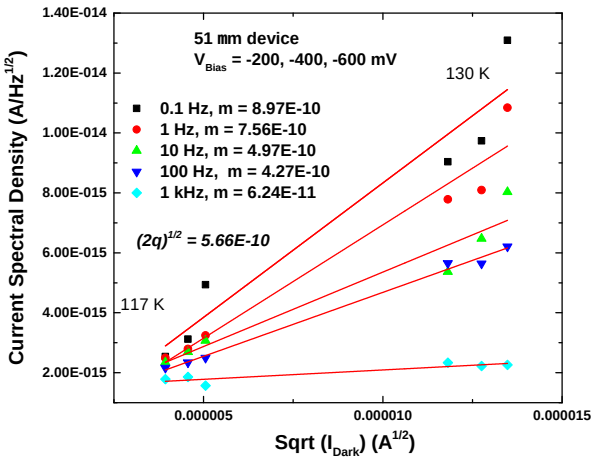

Figure 4.13: Pre-rad nBn noise vs the square root of the dark current over the diffusion-limited biases showing that the slopes are within about 35% of what would be expected for pure shot-noise.

The noise values at 0.1, 1, 10, 100, and 1000 Hz were found for the 51 μm device for the biases of -200, -400, and -600 where the devices appeared to have the highest diffusion current percentage. The noise values were plotted against the square root of the dark currents and the slopes were compared to the expected value for pure shot noise of $\sqrt{2q}$. The results showed a slope within 35% of the expected shot-noise value for frequencies of 1, 10, and 100 Hz. The 0.1 Hz data slope was about 58% higher and the high frequency, 1 kHz, slope was nearly an order of magnitude lower as expected from the drop off in the spectra shown in figure 4.11.

From the post-irradiation radiometric characterization results, it was clear that the current became more G-R dominated. In order to see the affect this change in current had on the noise, PSDs were collected after the exposure of the device to 63 MeV protons. Figure 4.14 shows the 51 μm noise spectra at 160 K for both pre and post-irradiation conditions on the same scale to more clearly demonstrate the change. Since the dark current and slope of the IV curves increased after dosing, the estimated noise was greater as illustrated by the horizontal lines in the post-irradiation case. The post-irradiation noise spectra not only increased to the level of

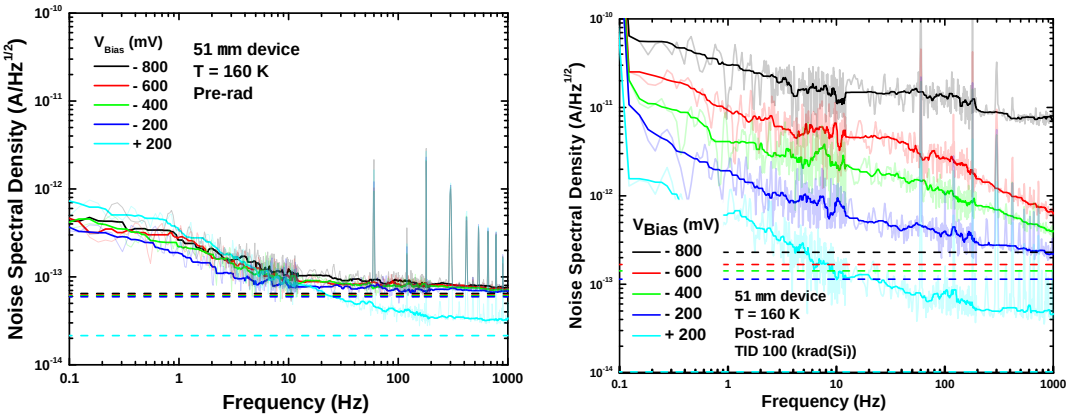

Figure 4.14: Noise PSD for a 51 μm nBn device at 117 K using a feedback resistor of 1 GΩ. The shot calculated shot and total noise are shown as dashed and solid horizontal lines respectively. $1/f$ and $1/f^{1/4}$ slope lines are included for illustration.

the newly estimated noise but far exceeded it. At low-frequencies, the actual noise exceeded the estimate by as much as two orders of magnitude post-irradiation. The same can be seen in figure 4.15 for the 201 μm device. This gives likely indication that the increase in G-R current of the nBn detectors resulted in an increase in $1/f$ like noise. The linkage between the G-R current and the $1/f$ noise was further supported by noise analysis of the ICIP detectors presented in the sections that follow.

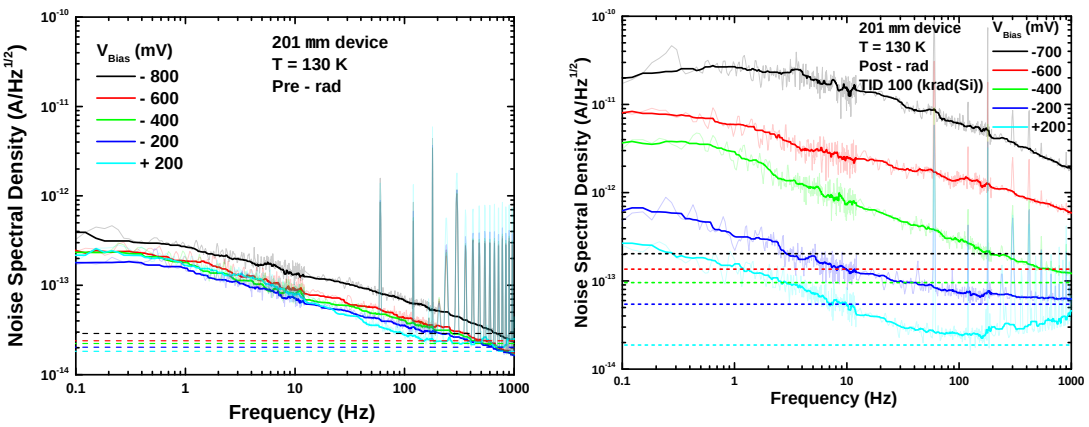

Figure 4.15: Noise PSD for a 51 μm nBn device at 117 K using a feedback resistor of 1 GΩ. The calculated shot and total noise are shown as dashed and solid horizontal lines respectively. $1/f$ and $1/f^{1/4}$ slope lines are included for illustration.

4.2 ICIP Characterization

This section details the radiometric, noise, and circuit stability analysis of the ICIP devices. Where possible, comparisons are made between the devices with a single or multiple stages.

4.2.1 Dark Current and Arrhenius Analysis

First, the electrical performance of the devices with 1, 4, 6, and 8 stages were measured at 80 K to 250 K in temperature steps that would be approximately evenly spaced in inverse k_BT space for further Arrhenius analysis. The IV curves for devices are shown in figure 4.16.

The high slopes in the IV curves in figures indicate that all of the devices were likely tunneling limited at temperatures less than 150 K which is consistent with results on devices from the same wafers presented in reference [13]. Arrhenius analysis was used to verify the visually apparent finding. The 1 and 4-stage IV curves at high temperatures showed what appeared to be the shallowest slope at 70 mV reverse bias so this was chosen as the bias at which to conduct the Arrhenius analysis. The dark current vs the inverse k_BT product is shown in figure 4.18.

To extract the different dark current components, the curves were fit using

$$I = A\exp(\frac{-qE_g}{k_BT}) + B\exp(\frac{-qE_g}{2k_BT}) + C, \tag{4.4}$$

where the first term represents the diffusion current component exponentially related to the full bandgap energy E_g, the second term represents the G-R current component exponentially related to half the bandgap energy, and the final constant term represents the temperature-independent current contribution which can be the result of a surface/shunt current or tunneling current. The bandgap energy was left

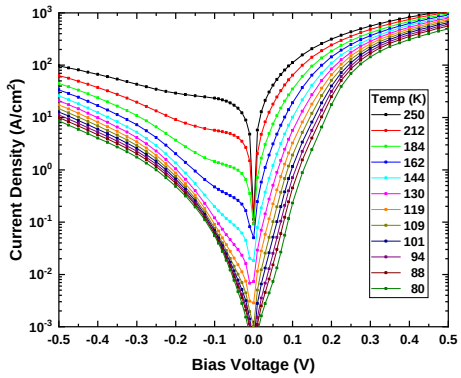

(a) 1-stage

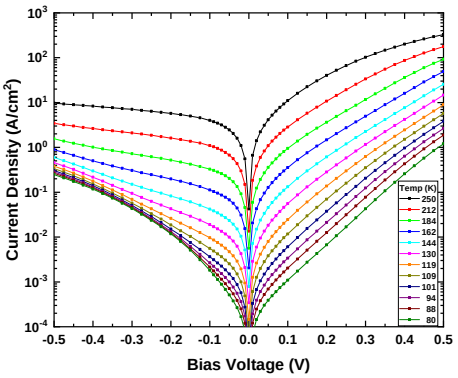

(b) 4-stage

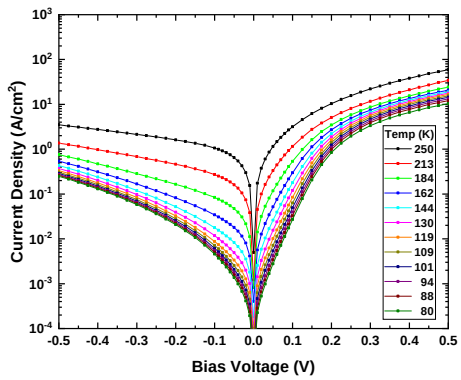

(c) 6-stage

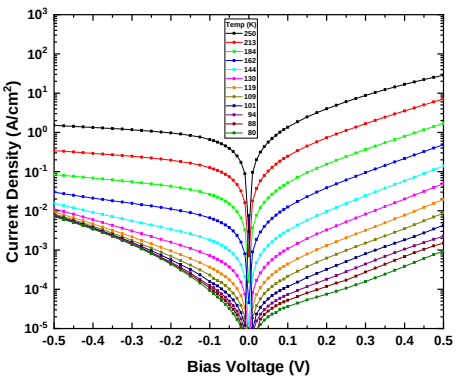

(d) 8-stage

Figure 4.16: IV curves of the ICIPs with 1, 4, 6, and 8 stages at temperatures from 80 to 250 K.

as a fitting parameter for all of the fits. The resulting parameters are summarized in the table below.

Device	E_g (meV)	A (A)	B (mA)	C (μA)
1-stage	183	2.3	3.2	0.26
4-stage	177	0.24	0.78	0.01
6-stage	196	0.16	1.1	0.21
8-stage	193	0.12	0.29	0.01

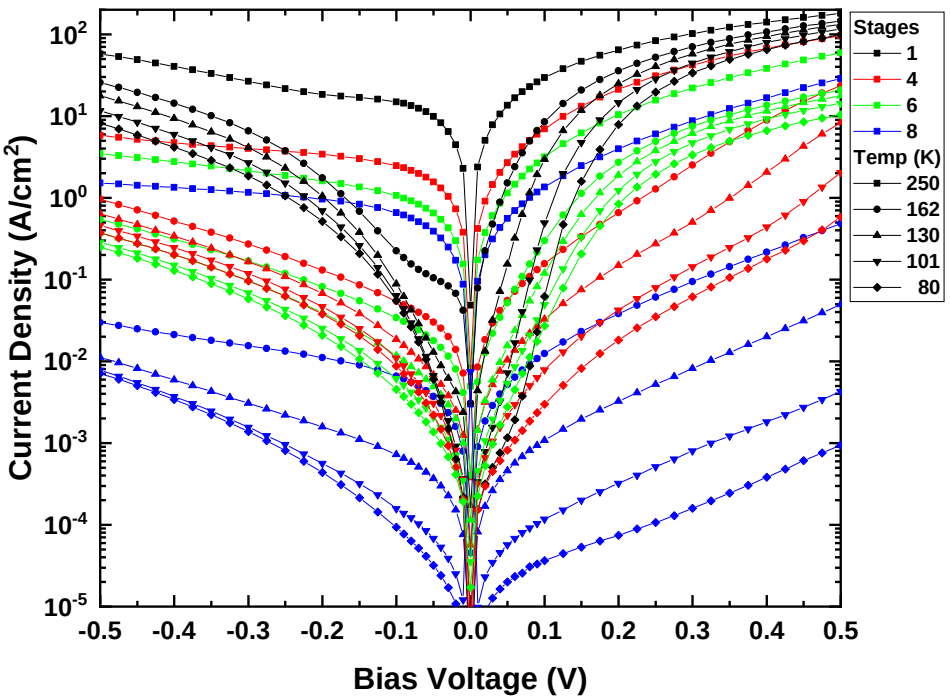

Figure 4.17: Dark current density vs voltage curves of the 1, 4, 6, and 8-stage ICIPs at selected temperatures.

After fitting the curves for both devices, the resulting currents due to each term were divided by the total current to show the percentage contribution of each current type. Figure 4.19 shows the diffusion, G-R, and temperature-independent percentages vs device temperature. In the 1-stage data, G-R current dominates between about 110 K and 160 K before tapering to about 10% and 5% at 250 K and 300 K respectively. For the 4-stage device, the G-R component dominates in the range from about 100 to 180 K and tapers to about 15% at 250 K. In the 6 and 8-stage devices, the G-R current appears to dominate starting at about 135 K and 118 K respectively. In the the 6-stage device, the G-R component is only overtaken by diffusion near 230 K, which is much higher than for the other devices. For the 8-stage, the same transition happens near 185 K. Looking back at the actual fits themselves

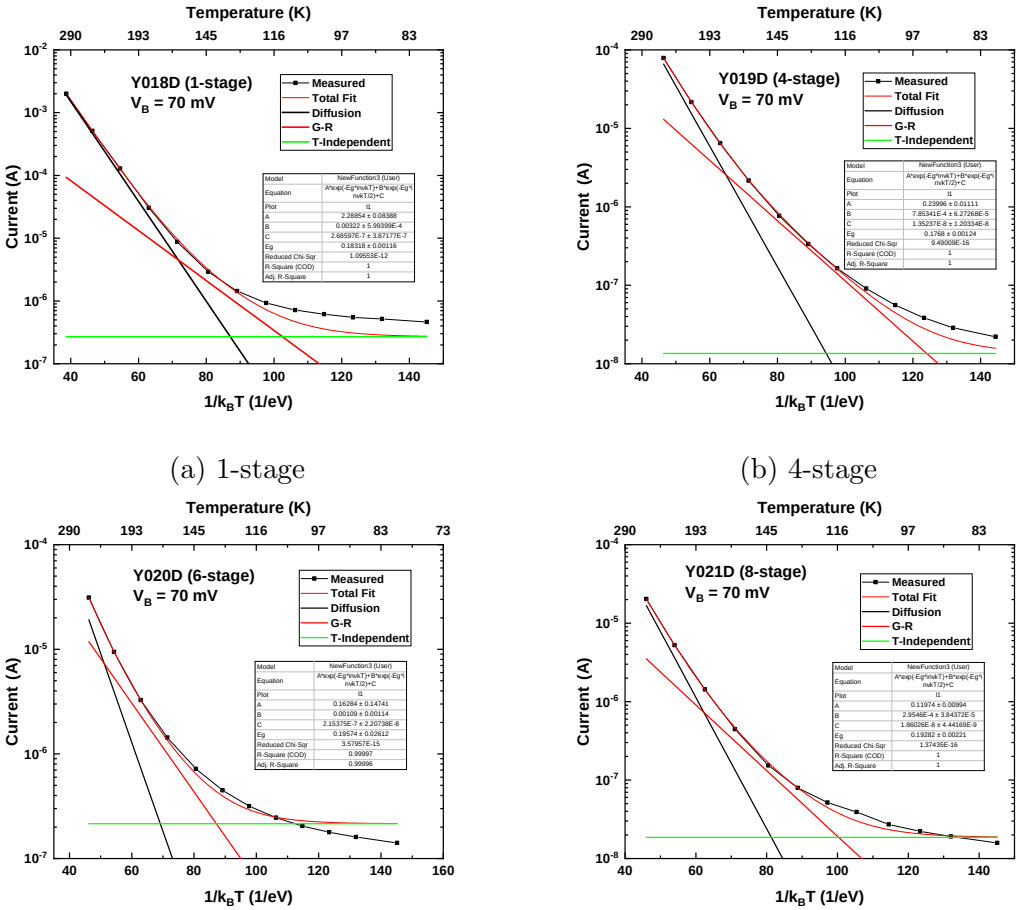

(a) 1-stage

(b) 4-stage

(c) 6-stage

(d) 8-stage

Figure 4.18: Arrhenius fits of the ICIPs with 1, 4, 6, and 8 stages to determine the diffusion, G-R, and temperatures independent contributions to the dark current.

in figure 4.18 and table 4.2.1 it is apparent that the goodness of fit for the 6-stage data is the worst. The temperature-dependent portion is fit to be about twice the minimum (low-temperature) current which cannot be physical.

The dark current density values were compared to the Rule 07 values for comparable cutoff wavelengths and operating temperatures. Figure 4.20 shows the dark current density curves of the 1-stage and 4-stage devices normalized to their Rule 07 values. At 80 K, both devices have dark currents multiple orders of magnitude higher than Rule 07. At 250 K, the 1-stage device has dark current 2 to 10 times

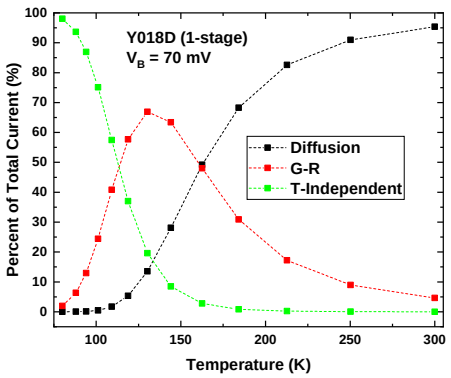

(a) 1-stage

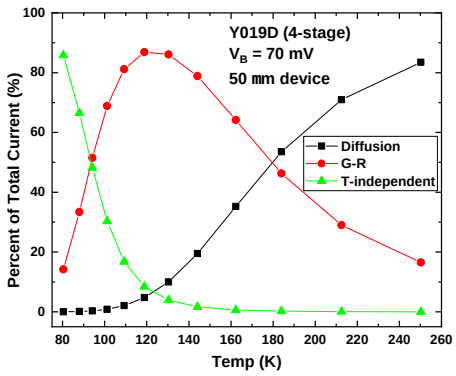

(b) 4-stage

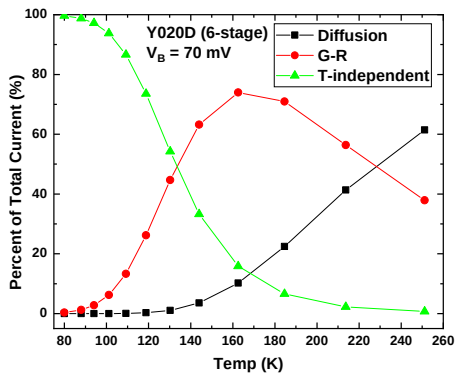

(c) 6-stage

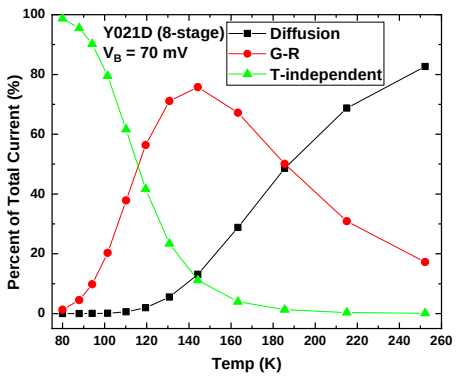

(d) 8-stage

Figure 4.19: Current component percentages vs temperature calculated from Arrhenius fits for the ICIPs with 1, 4, 6, and 8 stages.

the Rule 07 value in the bias range from 50 to 500 mV. The 4-stage device is less than the Rule 07 value, showing a factor from 0.2 to 1 over the same biases. If the quantum efficiencies and noise figures were comparable, the 4-stage device would show a marked advantage due to its low dark current. However, the 4-stage device was shown to have a quantum efficiency of about 4 times lower than the single stage device.

In addition to the comparisons of dark current as a function of bias and temperature, a dark current density vs perimeter to area ratio (P/A) plot was made for all

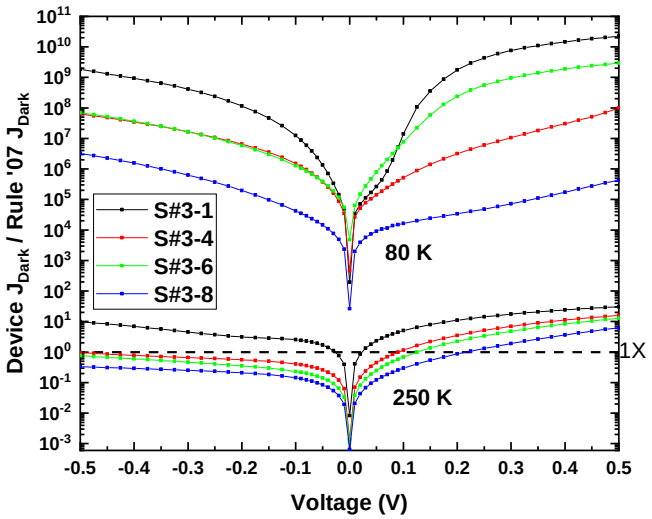

Figure 4.20: Dark current density vs bias plots as a multiple of Rule 07 values for the 1, 4, 6, and 8-stage devices.

four PECs to determine the affect, if any, of the surface current. One would expect that if there is a significant surface current in the devices, that the dark current density would be greater for smaller devices where P/A is larger. Figure 4.21 shows the dark current density at 80 K and a bias of 70 mV for devices ranging from 50 to 1000 μm plotted as a function of the individual devices' P/A ratio. All of the architectures (1, 4, 6, and 8 stages) are represented in the figure.

A linear slope upward (left to right) on the plot would indicate a significant and consistent surface current contribution to the current but for all four architectures there is no such trend. The 1-stage devices have a relatively flat curve with slightly higher calculated dark current densities at lower P/A ratios. The 4-stage devices show a similar but even more pronounced trend wherein the large devices (lower P/A) demonstrate the largest dark current density. The 6-stage devices are more scattered with notable outliers for the 200 and 500 μm devices. The 8-stage devices show higher dark current densities for the largest and smallest devices with the

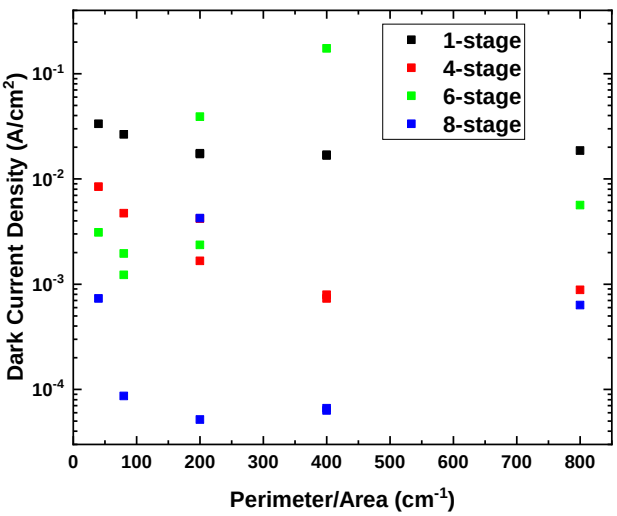

Figure 4.21: Dark current density vs perimeter to area ratio at 80 K and a bias of 70 mV for devices ranging in size from 50 to 1000 μm from ICIP PECs with 1, 4, 6, and 8-stage devices.

middle sizes having the lowest. It is possible the passivation was not consistent and that there may be shunt current sources contributing to some but not all of the devices on a given PEC regardless of size. The P/A analysis show at least that a perimeter surface current is not a dominant current source even in the small devices.

The NDC features of the ICIP devices are not apparent in the IVs at temperatures up to 250 K. To clearly see the NDC regions, the 6-stage device was tested in background limited conditions (dewar uncooled) at room temperature operation. Figure 4.22 shows the resulting IV curves with clear NDC features much like those illustrated in figure 2.4 related to RTDs. The number of NDC features corresponds to the 6 stages of the device and appear at biases in the 500 μm device of approximately 0.25, 0.45, 0.65, 0.9, 1.15, and 1.45 V. Taking the derivative of the IV curves yields the conductance (per unit area) vs bias of the devices. The result is plotted in figure 4.23 where the negative peaks are clear. This data is in good agreement with

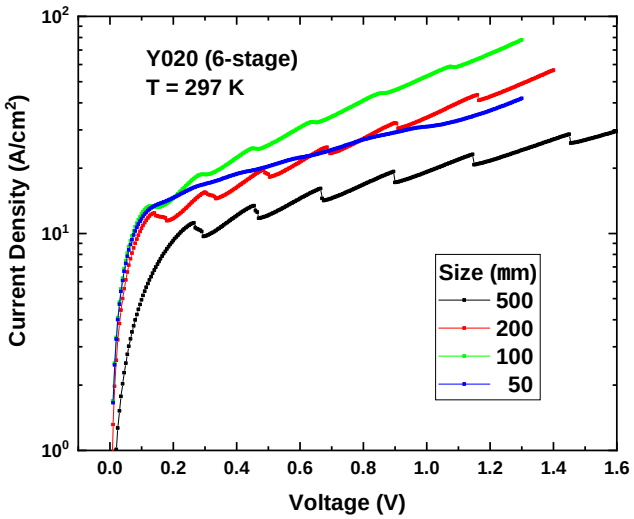

Figure 4.22: Dark current density vs bias plot of the 6-stage ICIP demonstrating six NDC peaks due to resonant tunneling.

that found in reference [23]. Here, it is shown that the NDC peaks occur at higher biases for the large devices and that the peaks themselves appear narrower. Further exploration of the photoresponse and noise near the NDC peaks is discussed in the following sections.

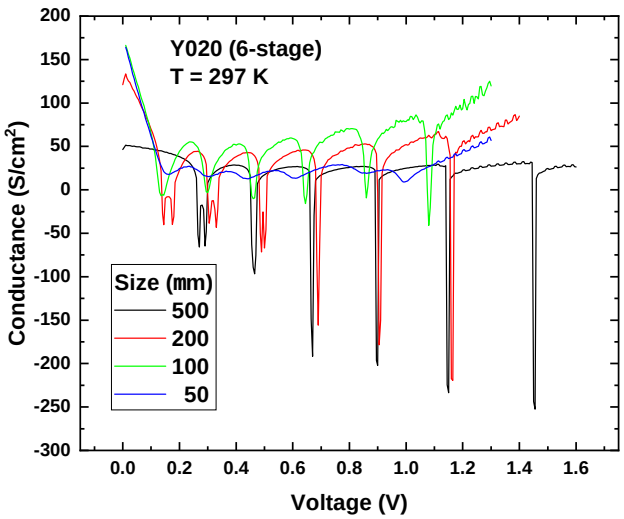

Figure 4.23: Conductance vs bias plot of the 6-stage ICIP demonstrating six NDC peaks due to resonant tunneling.

4.2.2 Photoresponse and Quantum Efficiency

The absorption spectra of all four ICIP devices were measured in the small blue dewar in the configuration described in section 3.2.1 with an FTIR. The spectra for the the 1, 4, 6, and 8-stage device are shown in figure 4.24 at 80 to at least 250 K. For the 1-stage device, the spectra appear smooth through an operating temperature of 200 K. The 250 K spectrum appears noisy indicating a low SNR at this temperature due to either low photocurrent, high dark current, or a high noise current. The absorption spectra for the 4-stage device appear relatively smooth through an operating temperature of 250 K. Even the 280 K spectrum is smoother than the 250 K spectrum of the 1-stage device. This provides some indication that the 4-stage device offers an advantage at higher temperatures. The same is true of the 6 and 8 stage devices which maintain a relatively smooth spectrum through 250 K. It is unclear from this data alone whether the better high temperature performance is due to the multiple stage architecture or is just due to having shorter individual

absorbers. Put another way, it's possible that a 1-stage device with a shorter absorber could have maintained photocurrent better than the given 1-stage device at higher temperatures simply due to the latter being affected by a degraded diffusion length.

The inflection points of the spectra were used to determine the cutoff wavelengths. Figure 4.25 shows the cutoff wavelengths for both devices versus temperature. The cutoff wavelengths were relatively consistent between devices over the full range of temperatures tested. After completing spectral response measurements, the inner cold shield was installed in the small blue dewar with a pinhole of 0.8" and a spectral bandpass filter spanning from 4650 to 5300 nm. A chopped, 900 K blackbody was placed in front of the dewar window and the photocurrent was measured for the devices using a lock-in amplifier. The photocurrent vs bias curves are shown for all the ICIP devices in figure 4.26. The plots show that the photocurrent is independent of bias near zero bias. At higher bias in both forward and reverse directions, the photocurrent became very noisy. In order to calculate the quantum efficiency of the devices, the zero-bias photocurrent was plotted as a function of device area and then fit using the following function

$$I_{ph} = q\eta E_q A_d = q\eta E_q (L_{nom}^2 + 4L_{OC}L_{nom} + \pi L_{OC}^2), \tag{4.5}$$

where the effective device area A_d is made up of both the nominal device area L_{nom}^2 and the area around the device within one lateral optical collection length L_{OC}. The photocurrent vs device length and resulting fits are shown in figure 4.27. From these fits, the external quantum efficiencies were found to be approximately 20.6%, 4.9%, 4.6%, and 3.4% for the PECs with 1, 4, 6, and 8 stage ICIPs respectively. Since the measurements were taken at 80 K where any limitations imposed by a degraded diffusion length were eliminated, the multi-stage devices were expected to have lower quantum efficiencies due to their shortened absorbers.

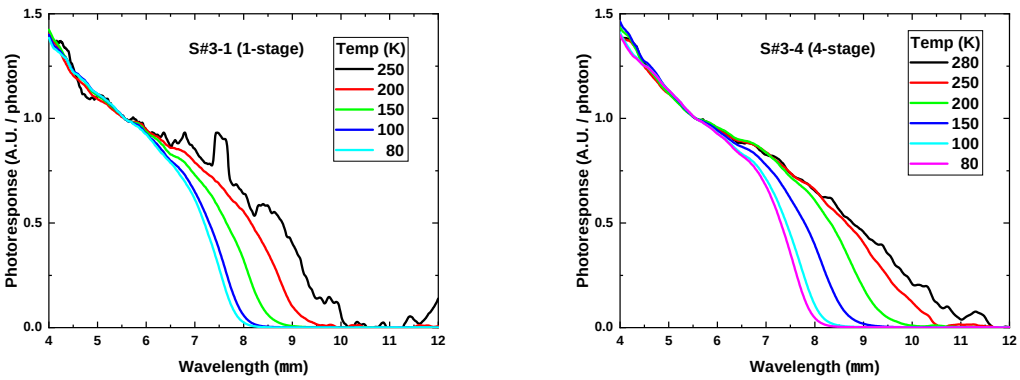

(a) 1-stage

(b) 4-stage

(c) 6-stage

(d) 8-stage

Figure 4.24: Absorption spectra for the four ICIP devices with different number of stages. Note that the single stage device spectra is noisy at 250 K while the others are not.

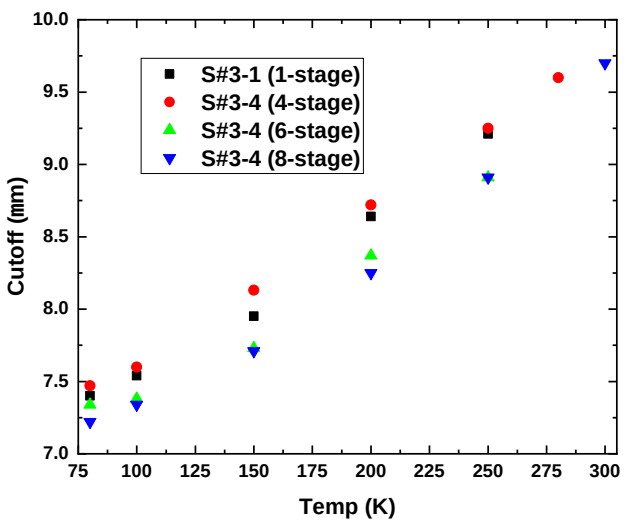

Figure 4.25: Cutoff wavelengths of the devices as a function of temperature.

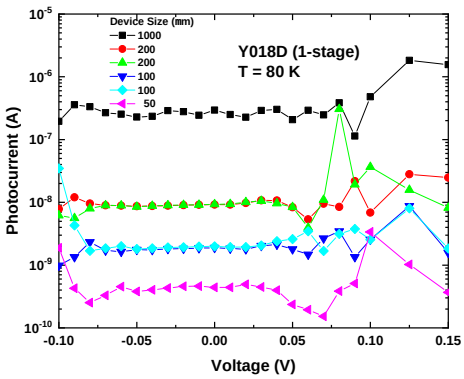

(a) 1-stage

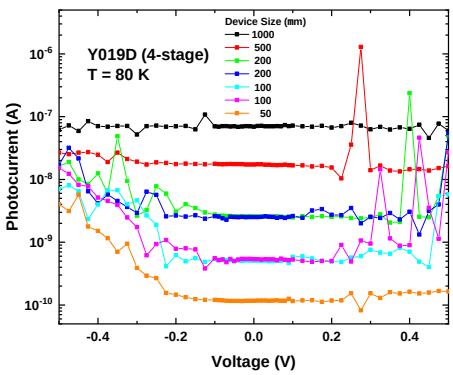

(b) 4-stage

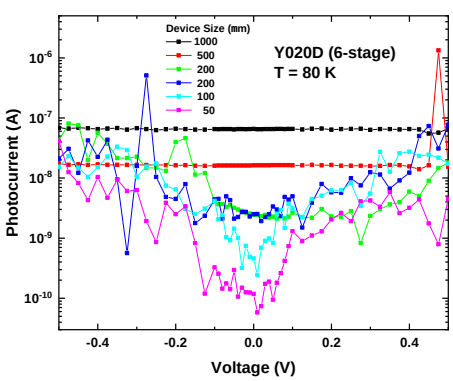

(c) 6-stage

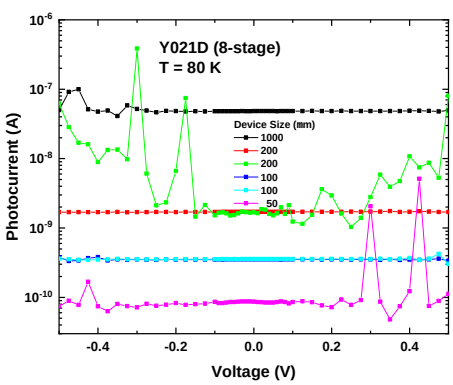

(d) 8-stage

Figure 4.26: Photocurrent vs bias for multiple sizes of ICIP detectors from the PECs with (a) 1-stage, (b) 4-stages, (c) 6-stages, and (d) 8-stages .

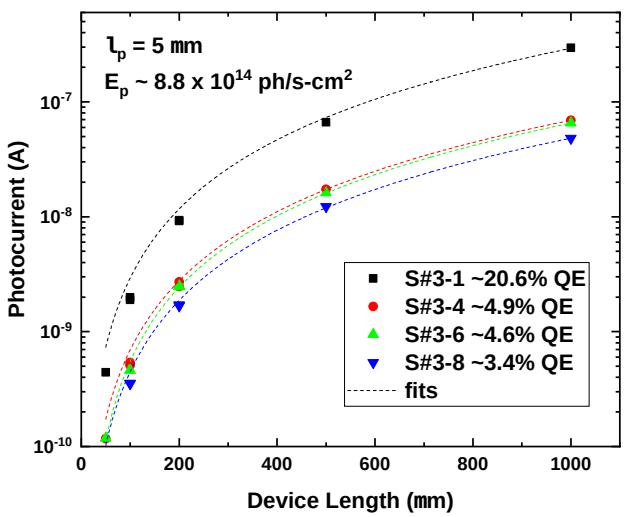

Figure 4.27: Photocurrent vs mesa length at zero bias and 80 K for the 1, 4, 6, and 8-stage ICIP PECs.

4.2.3 Noise Power Spectral Density

Noise spectra were collected in both the dedicated noise dewar with internal TIA and the blue dewar with an external TIA under varying temperature and bias conditions for the 1, 4, 6, and 8-stage devices. Before presenting the actual data, it is important to consider what the ideal data would look like in order to confirm the theoretical noise gain of ICIPs presented in chapter 2. It was expected that all of the devices would have some level of $1/f$ or other low-frequency noise above the white-noise level estimated using by equation 2.37. There was expected to be a corner frequency above which the white Johnson and shot noise contributions would dominate. In order to isolate the shot noise component, one technique is to increase the photon flux incident on the device so that the overall current increases without the $1/f$ component increasing. Figure 4.28 shows what ideal noise spectral results would look like to allow identification of the shot noise gain term.

In this figure, the $1/f$ component remains constant as the white noise increases

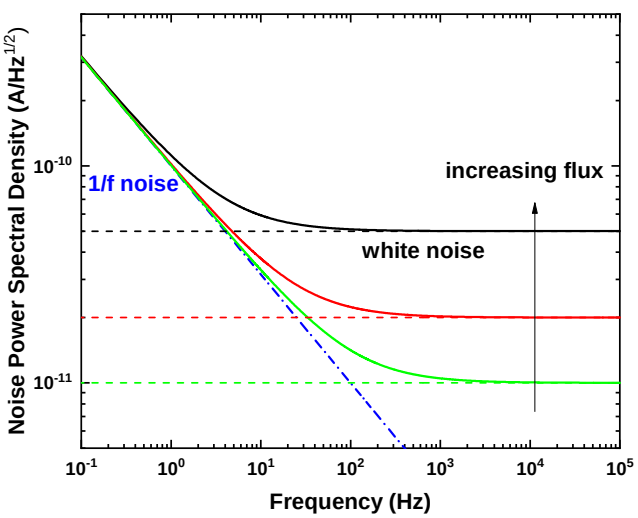

Figure 4.28: Ideal noise spectra of a device at different illumination levels.

with increasing photogenerated current. The shot noise gain, g_n could be determined by the following relation

$$g_n = i_{n,white}/\sqrt{2qI}, \tag{4.6}$$

which could be found for the individual measurements or by fitting a plot of i_n vs the square root of the current as was done in figure 4.11 where the shot noise was identified in the nBn device pre-irradiation. The results that follow for the various ICIP architectures show that for no temperature or bias regime was a white noise portion of the spectrum clearly visible.

Noise spectra were first collected in the dedicated noise dewar with the internal TIA on the 1-stage device. Figure 4.29 shows the noise spectra for the 1-stage device at 80 K as a function of bias. 80 K was initially chosen to reduce the overall dark current as much as possible. From the figure, it is apparent that a flat portion of the spectrum was not reached for any of the biases tested. All of the spectra contain a peak near 40 kHz which was not linked to a physical source in these measurements.

After the initial noise measurements of the dark current, the shutter was open and a 1200 K blackbody was placed in front of the dewar. Noise measurements were repeated under illumination and the resulting spectra are shown in figure 4.30.

The preceding findings for the 1-stage device indicated that operating at 80 K where the device was tunneling or shunt current-limited was leading to such a high $1/f$ noise component that the shot noise was not visible even at high frequencies. Unfortunately, it was not possible to operate at much higher temperatures before saturating the op-amp even with the smallest feedback resistors available (the lowest gain). Thus, in an effort to test at the highest temperature, the 8-stage device was loaded into the noise dewar since it had the lowest overall dark current. It was tested up to a temperatures of 120 K. Noise measurements were taken from 0 to 700 mV

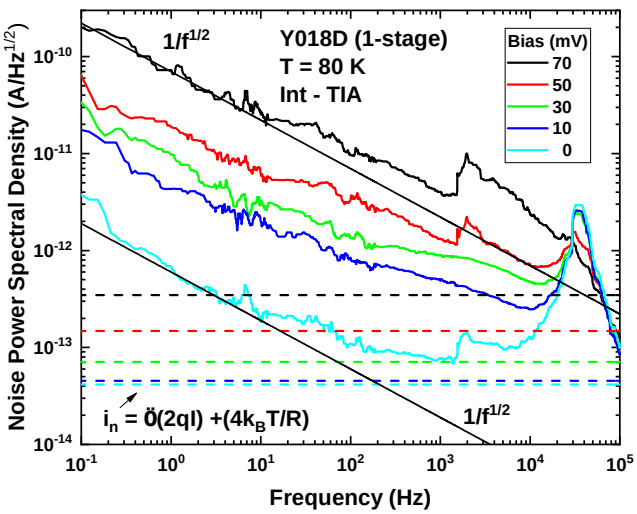

Figure 4.29: Noise spectral measurements for the 1-stage device at 80K for biases from 0 to 70 mV with no blackbody illumination. The figure includes the calculated total noise (shot plus Johnson) as well as $1/f^{1/2}$ lines.

at 80 to 120 K. Figure 4.31 shows the 80 K noise spectra for the 8-stage device up to 700 mV bias.

Since the noise in these devices was so much higher than anticipated, it was hypothesized that it might be possible to obtain accurate noise measurements in the small blue dewar with the external TIA that could provide a gain as low as 10^3 V/A so that higher temperatures could be reached.

Noise spectra were collected on the 1-stage and 4-stage devices first in the blue dewar at temperatures from 80 to 250 K. A bias of 70 mV was used corresponding to the shallowest portion of the IV and to the bias at which the preceding Arrhenius analysis was completed. Figures 4.32 and 4.33 show the noise spectral density plots for 1-stage and 4-stage devices respectively.

Over the full temperature range, both devices demonstrate a clear $1/f^{1/2}$ fre-

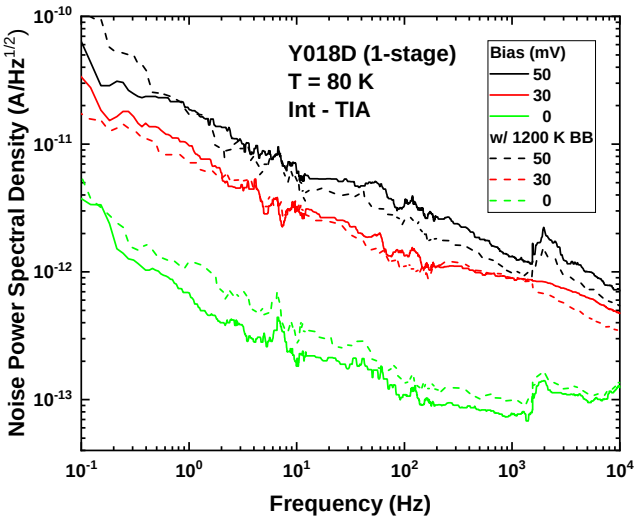

Figure 4.30: Noise spectral measurements for the 1-stage device at 80K for biases from 0 to 50 mV with and without blackbody illumination. The spectra were mostly unaffected by the additional photogenerated current.

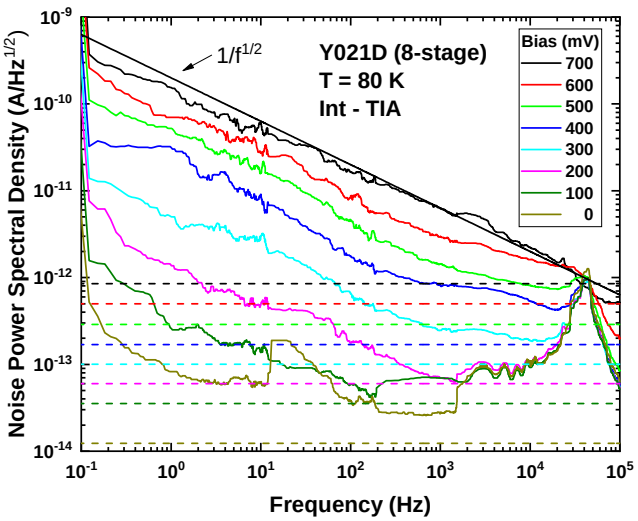

Figure 4.31: Noise spectral measurements for the 8-stage device at 80K for biases from 0 to 50 mV.

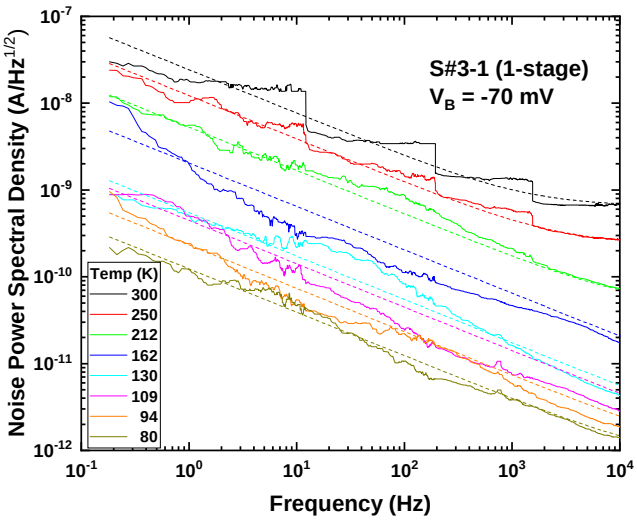

Figure 4.32: Noise spectra for the 1-stage device at 70 mV reverse bias from 80 to 250 K. The steps visible in the higher temperature spectra are the result of DC saturation of the spectrum analyzer.

quency dependence with almost no flattening up to 10 kHz. Considering the scales of the two figures, it is apparent that the 4-stage device has lower noise for each operating temperature. If the $1/f$ noise is proportional to the device current as has been demonstrated in other work, the result was expected due simply to the lower dark current of the 4-stage device. In order to make comparisons between the two device's noise performance, a few things must be considered. The first is how well the actual device noise relates to that estimated by equation 2.37. This involves normalizing the curves to the estimated values. The second comparison method is to see how the noise relates to the current of the device. One established method of doing this is to determine the Tobin coefficients of the devices as discussed in section 2.7.6.

Following the first method of comparison, the noise spectra of both devices were divded by the white noise from equation 2.37. The resulting normalized spectra are

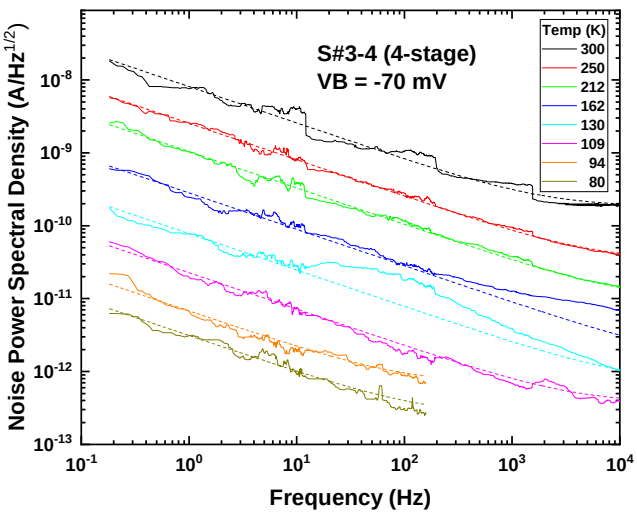

Figure 4.33: Noise spectra for the 4-stage device at 70 mV reverse bias from 80 to 250 K. The steps visible in the higher temperature spectra are the result of DC saturation of the spectrum analyzer.

shown in figure 4.34. For all of the temperatures presented, the 4-stage device had a lower normalized noise. The result here suggests that while both devices will have greater noise than that typically estimated and used in the calculation of detectivity, the error in the estimate is larger for the 1-stage device than for the 4-stage. It appears that this is especially the case at lower temperatures (80 K) where the 4-stage device is about 30 times the estimated noise at 1 Hz while the 1-stage is about 300 times the estimated noise. At higher temperatures, the difference between the estimated and the actual noise between the devices narrows to less than an order of magnitude.

Since the estimated noise scales with the square root of the current and the square root of the conductance (the inverse of the resistance), the above technique does not provide a complete comparison of the potential noise reduction resulting from additional stages in the ICIP architecture. To see if for a given current value

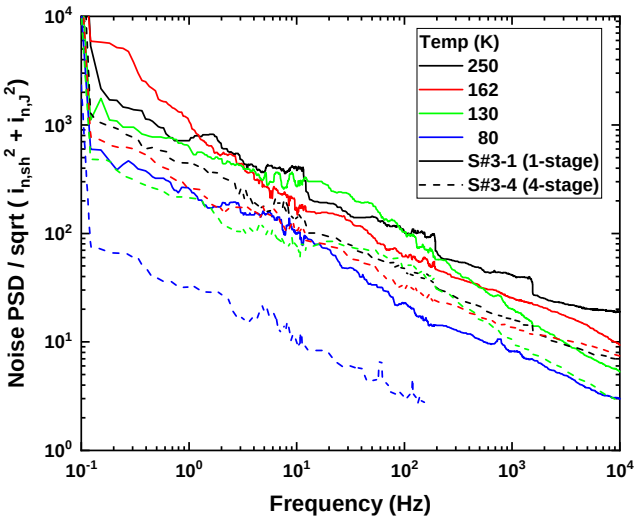

Figure 4.34: Noise spectral measurements for the 1 and 4 stage devices normalized to the total theoretical white noise given by equation 2.35. High frequency noise of the 4-stage device at 80 K was overcome by system noise and is not shown.

the multi-stage architecture offers an advantage, the Tobin coefficients must be compared.

The 1 Hz noise values were found for the devices operating at 70 mV and temperatures from 80 to 250 K. Figure 4.35 shows the resulting Tobin coefficients plotted vs temperature for the 1, 4, 6, and 8-stage 50 μm devices. The results reveal several noteworthy characteristics. The first is that all three devices show a similar temperature dependence wherein there is a peak in the Tobin coefficients between 100 and 140 K and a convergence toward zero at higher temperatures. The second feature shows that at temperatures at about 160 K and below, the 1-stage device has higher absolute Tobin coefficients. This means that for a given current value, the 1-stage device exhibits more $1/f$ noise. This suggests that at lower temperatures, the multi-stage architectures not only have lower dark current but they also have less noise per unit of dark current.

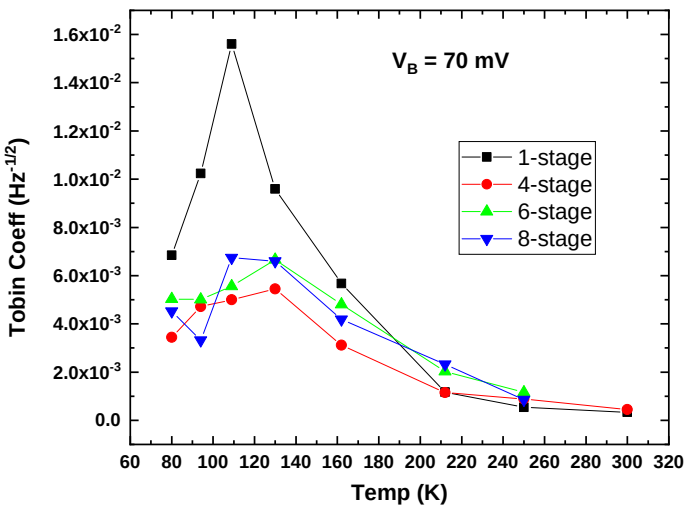

Figure 4.35: Tobin coefficients vs temperature for the 1, 4, and 6-stage devices.

The similar temperature dependence across the architectures provides some indication that the $1/f$ noise is related to a specific current mechanism in the ICIPs. Reviewing figure 4.19 shows that among the three current mechanisms (diffusion, G-R, and temperature-independent), the G-R component as a percentage of the overall current shows a very similar temperature dependence as the Tobin Coefficients in figure 4.35. This correlation of the $1/f$ noise to the G-R noise in the device is consistent with the findings in the irradiated nBn detector. The combined results indicate that G-R current should be carefully considered in developing and operating devices when attempting to minimize noise, either through optimizing growth and processing or by operating the devices in temperature and bias regimes where the G-R current is not dominant.

4.2.4 Negative Differential Conductance and Circuit Instability

In addition to the noise spectra taken as a function of temperatures and large bias steps, noise measurements were also collected on the 6-stage device operating at room temperature in finer bias steps near the first NDC peak. As was shown in figure 4.22, the first peak appeared at a bias of 0.25 V. Figure 4.36 shows noise spectra for biases before, through, and after the apparent NDC region. The first notable result is that there is no substantial difference in the noise spectral shapes at frequencies up to about 5 kHz between the biases with positive and negative differential conductance. This provides some indication that the resonant tunneling process itself is not a major contributor to the $1/f$ noise in as far as it is not greater than the $1/f$ noise suspected to be linked to the G-R current. The second notable result is the distinct peaks between 50 kHz and 90 kHz that are only present in the NDC region. There is no peak for biases just before or after the NDC. The narrowness of the peak indicates a relatively clear oscillation frequency.

To further explore the noise behavior near the NDC peak, the output signal of the device was fed into an oscilloscope and the time-domain signal was captured. Figure 4.37 shows the resulting AC signals for different bias steps before, during, and after the NDC. The plots corroborate the clear frequency oscillation indicated by the PSDs. The oscillation periods are about 2.6 μs which corresponds to a frequency of about 385 kHz. Referring back to figure 4.36, it is apparent that there is not an exact frequency match to the 50-90 kHz peaks shown which would correspond to a period of about 1.6 μs. The cause of this difference is yet unknown but is expected to be a result of the exact circuit configurations involved in the two tests. Regardless, the oscillations are similar to those found in the work of Kidner et al wherein the negative differential conductance in circuits containing RTDs lead to oscillatory signals.[25] This leads to the conclusion that the oscillations are a manifestation of the negative

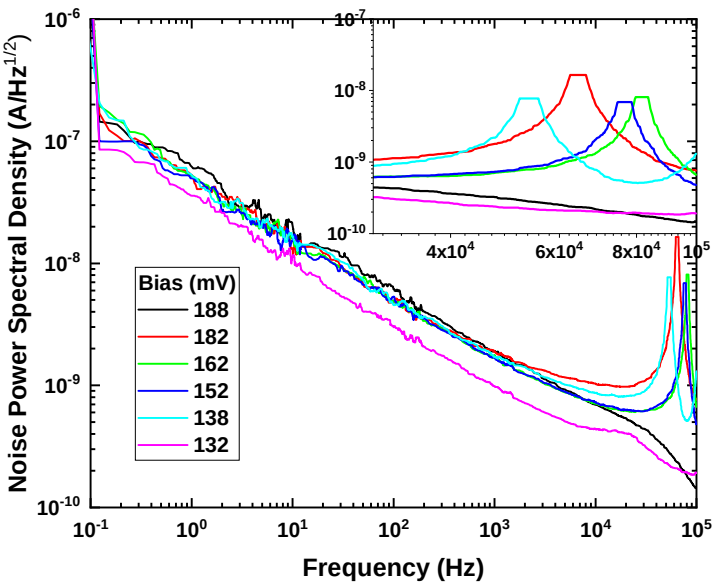

Figure 4.36: Noise spectra of the 6-stage ICIP operated at room temperature with biases before, during, and past the NDC region

resistance interaction with the full circuit rather than manifestations of oscillations in the device structure alone.

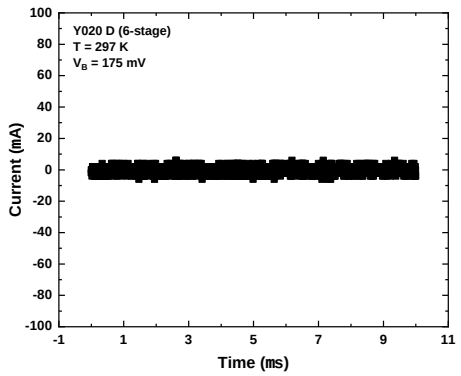

(a) Pre-NDC

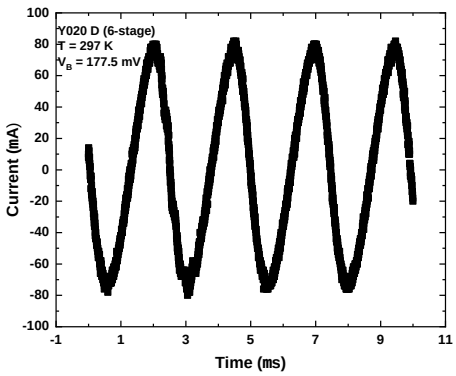

(b) Begin NDC

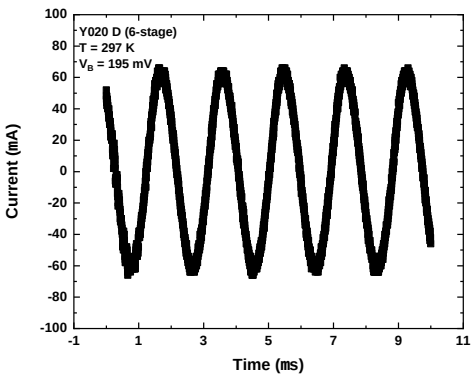

(c) Peak NDC

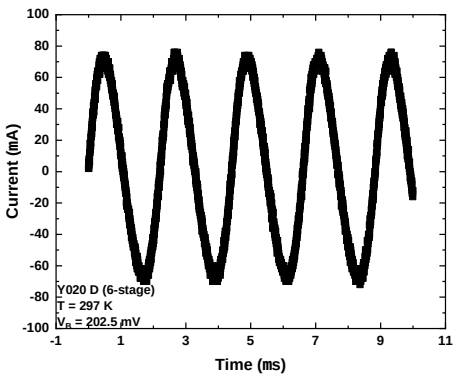

(d) Near end NDC

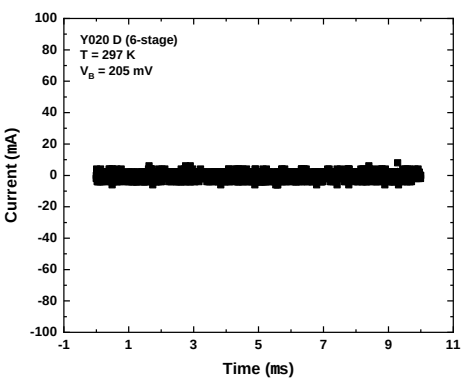

(e) After NDC

Figure 4.37: Time domain signal of the 6-stage device at room temperature in the region of the first NDC peak.

4.2.5 Photocurrent Gain

The blackbody at 1200 K used to illuminate the devices did not provide enough flux to make the photocurrent clearly distinguishable from the dark current when the device was operated at room temperature. In order to clearly see the photocurrent while maintaining a high enough temperature to observe clear NDC regions in the IV, a 632 nm and a 1550 nm laser were used to illuminate the device. Figure 4.43 shows the room temperature dark current and laser-illuminated photocurrent of the 6-stage ICIP device. Two key findings are observed in the IVs. The first is that the laser-illuminated IV is very near the dark current for biases up to the point at which the resonant tunneling-induced NDC region begins. Throughout the NDC region, the laser-illuminated IV is significantly larger than the dark current. Plotting the difference of the two curves reveal what should be just the photocurrent in figure 4.43 and reveal an apparent photocurrent gain of 20X at the peak of the first NDC region. This figure also shows the result of adding the stabilizing capacitor which smooths the NDC region and makes the photocurrent gain region one peak rather than two. This method of stabilizing a circuit with NDC is discussed further in reference [25]. Distinct features appear in the second and third NDC regions where the photocurrent appears to be negative. This apparent negative photocurrent is explained by the second key finding. Upon closer inspection of figure 4.42, it is apparent that the laser-illuminated IV features are shifted to higher biases up to around 0.25 V and after that, the features appear shifted to lower bias when compared to the dark IV. This causes the photocurrent calculated from the subtraction of the two curves to appear negative for the second and third peaks when in actuality, the effective biases have shifted.

The apparent shift to higher bias near the first NDC and shift to lower bias for the subsequent stages agrees well with the theory that the stages of a non-current-matched multi-stage ICIP will distribute the bias amongst themselves in order to

establish equal currents as discussed in section 2.5. The results show here, using the NDC features, that this is likely the case.

Literature values for the absorption coefficient of a 10.5 μm cutoff InAs/GaSb superlattice absorber are between 0.07 and 0.3 μm^{-1} for a detector temperature of 77 K over the wavelength region from 4 to 10 μm.[49] At higher temperatures, the absorption coefficient was shown to increase as expected with a narrowing of the bandgap.[13] Absorption coefficients for the near-IR or visible wavelengths were not readily available. Extrapolating from the available absorption spectra and literature values, the absorption coefficient of the LWIR device at room temperature was expected to be on the order of 1 μm^{-1}.

Considering just the non-reflecting photons that penetrate into the device absorbing layers, the percentage of photons absorbed by depth can be found using[21]

$$P_{abs}(d) = 1 - e^{-\alpha d}, \tag{4.7}$$

where d is the depth into the absorbing layer. In the case of multi-stage ICIPs, the above equation does not account for any absorption in the other structure layers and the variable d does not represent the actual depth into the whole structure. Using equation 4.7 and α values ranging from 0.1 to 5.0 μm^{-1}, figure 4.38 shows the percentage of non-reflected photons that are expected to have been absorbed at varying absorber depths. The values are plotted out to the full absorber width of 2.293 μm for the 6-stage device.

Figure 4.38 shows that for MWIR and LWIR wavelengths with expectant absorption coefficients near 0.2 μm^{-1} only about 40 % of the penetrating photons are absorbed through the full depth of the distributed absorber. For visible and SWIR wavelengths, the photons are nearly all absorbed by the full absorber thickness and the majority of photons are absorbed in the first micron or less. By taking the

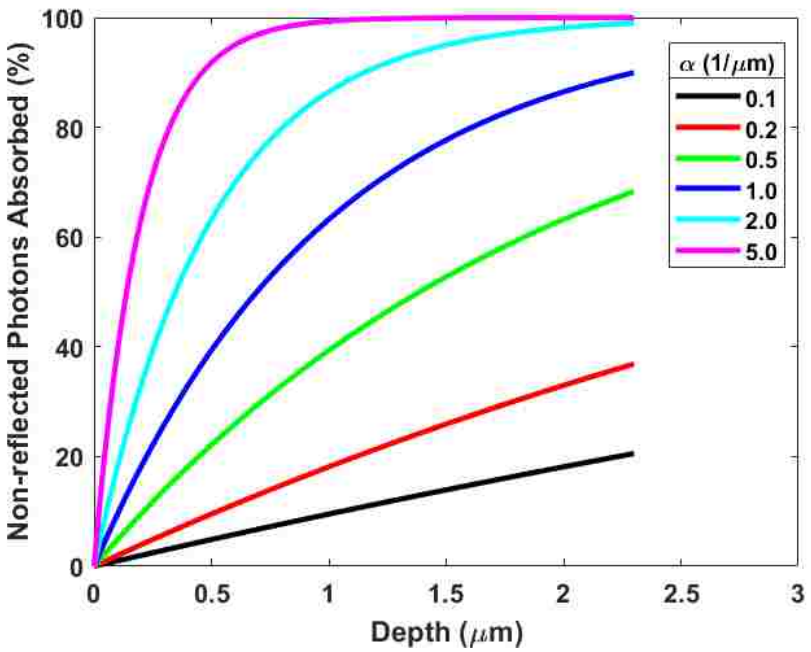

Figure 4.38: Percentage of the total photons absorbed in each of the stages of the 6-stage ICIP with varying absorption coefficients.

difference in photons absorbed at the beginning and end of each stage depth, the percentage of photons absorbed in a particular stage can be found. Figure 4.39 shows the percentage of non-reflected photons absorbed in each stage and figure 4.40 shows the percentage of the total absorbed photons each stage contributes to. The latter is found by dividing each stage's share of the photons by the total photons absorbed.

Figure 4.39 shows that the first stage absorbs between about 45 and 80 % of the photons for absorption coefficients between 2.0 and 5.0 μm^{-1}. The 632 nm and 1550 nm lasers used to illuminate the devices were expected to correspond to absorption coefficients in this range with that of the visible laser exceeding that of the SWIR laser. The visible wavelength laser is expected to have a short penetration depth in the LWIR detecting material given the above calculations and as such, the signal is attenuated greatly by the time the light reaches deeper stages. The first stage, then, produces the bulk of the current and accumulates holes that act as a sheet of positive

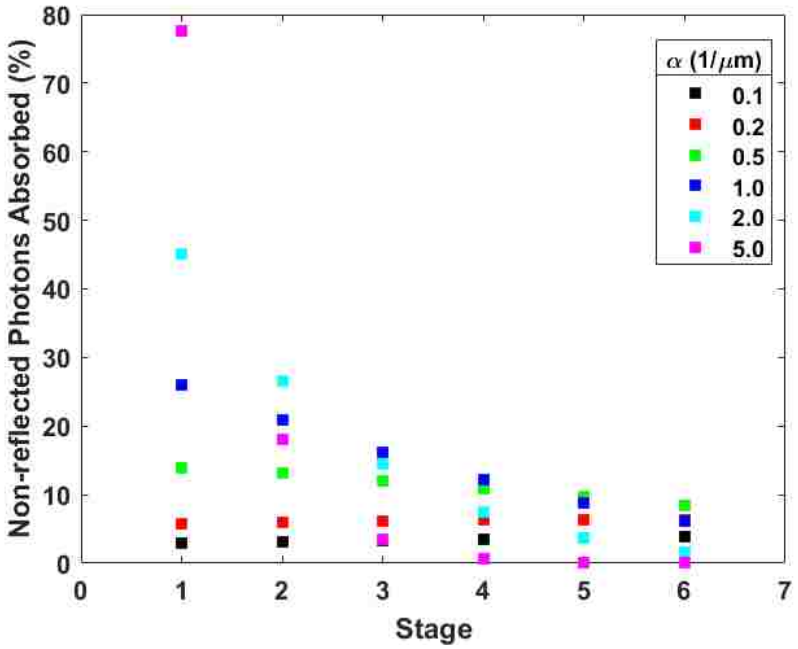

Figure 4.39: Percentage of the non-reflected photons absorbed in each of the stages of the 6-stage ICIP with varying absorption coefficients.

charge. This diminishes the field produced by the external bias in the first stage but increases the field in subsequent stages . Thus, the NDC features proved to be useful markers in the IV curves for directly demonstrating the effect of unmatched currents through the multiple stages. It is yet unclear, however, if this is the case, why the first electron barrier would see a different direction of the electric field contribution from the hole accumulation than the subsequent stages since it is also after the first absorber. Some speculation in earlier ICIP work was made that proposed that the resonant tunneling leading to the NDCs is actually a result of resonance within the quantum wells of the electron relaxation region (the hole barrier). [29] This has not been the more recent explanation in the literature which points to resonance in the electron barrier.[22, 23] The findings in this research through laser illumination and subsequent observation of shifts in the NDC peaks suggest that the phenomenon may be related to resonance in the hole barrier given that the first hole barrier in

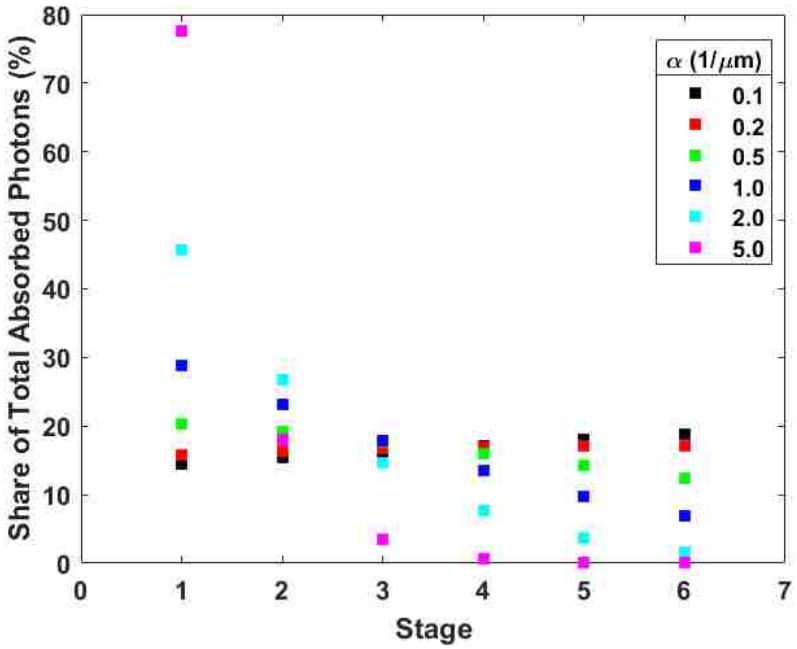

Figure 4.40: Percentage of the total absorbed photons absorbed in each of the stages of the 6-stage ICIP with varying absorption coefficients.

regularly illuminated devices is the only region before the first absorber that would experience an opposite electric field contribution due to hole accumulation than the rest of the device. An illustration of this is shown in figure 4.41 for the case where a high absorption coefficient leads to mismatch in the number of photons absorbed in each stage.

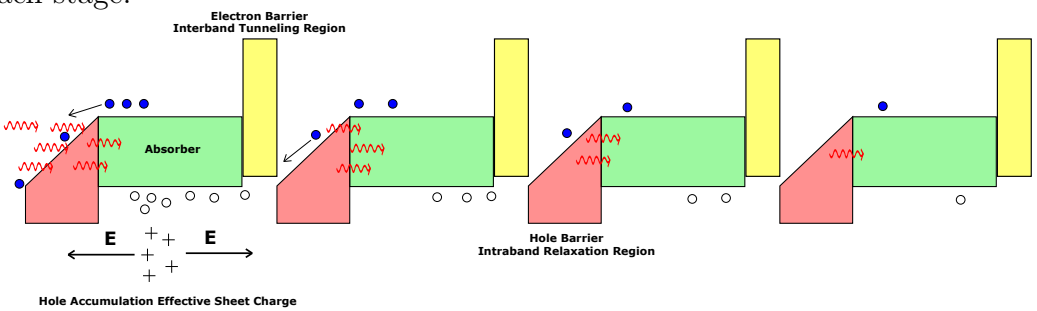

Figure 4.41: Illustration of the hole accumulation in the first ICIP stage as a result of the short penetration depth of the 632 nm laser.

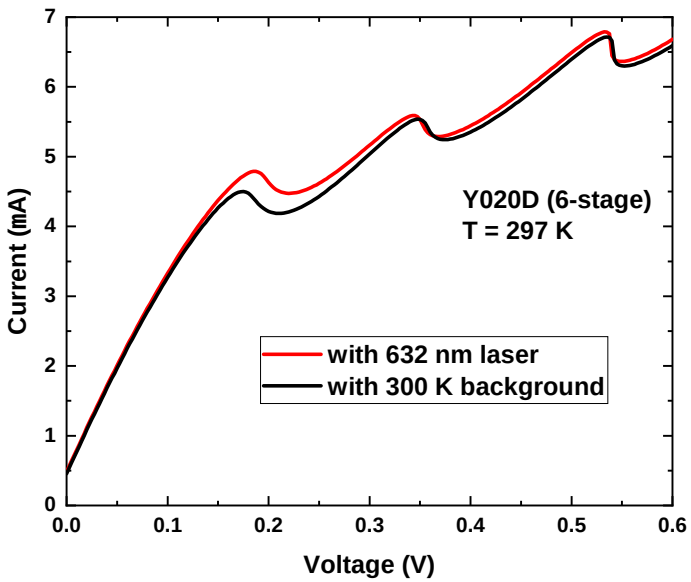

Figure 4.42: IV curves of the 6-stage ICIP device operating at room temperature exposed to room temperature background radiation and illuminated with a 632 nm laser.

To further explore the finding above, a 1550 nm laser was used to illuminate the device and once again, IV curves were taken with and without the laser. If the above hypothesis for the physical origins of the IV NDC feature shifts, the 1550 nm laser should cause more than the first peak to shift to higher bias due to its deeper penetration depth. The findings are shown in figure 4.44 where the DC IV curves are plotted with and without laser illumination. Figure 4.45 shows the difference between the two curves to reveal just the photocurrent. The results confirm the hypothesis that a longer wavelength laser would generate current more evenly among the initial stages of the device and therefore result in more than just the first NDC peak shifting to higher biases. The peak gain near the first NDC is about 10X.

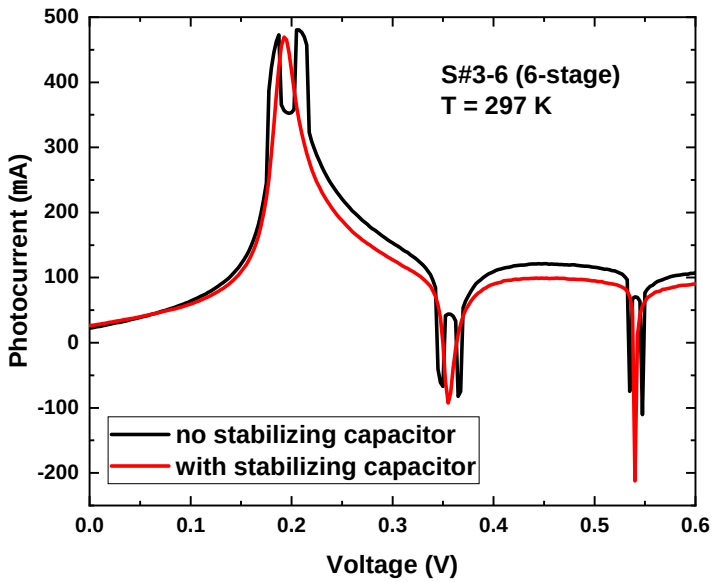

Figure 4.43: Photo-IV curve of the 6-stage ICIP device operating at room temperature illuminated with a 632 nm laser found by the difference in curves from figure 4.42.

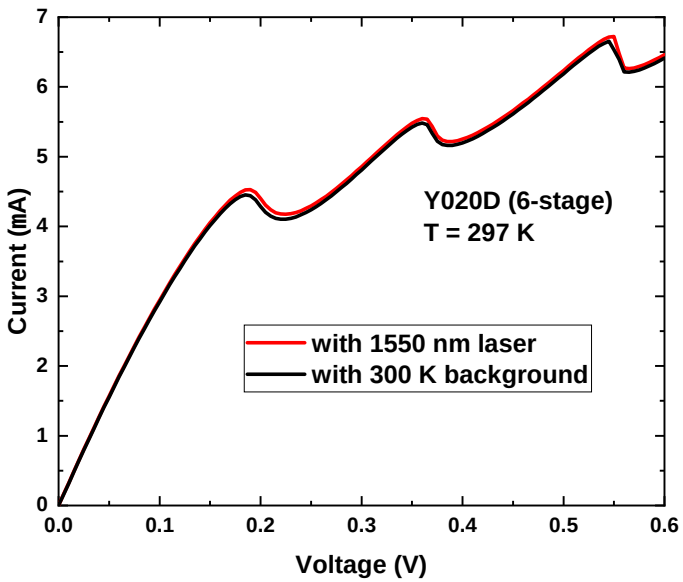

Figure 4.44: IV curves of the 6-stage ICIP device operating at room temperature exposed to room temperature background radiation and illuminated with a 1550 nm laser.

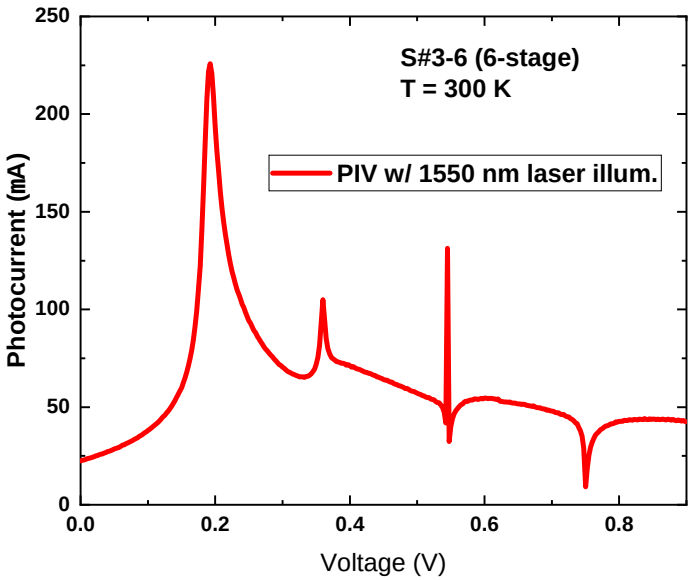

Figure 4.45: Photo-IV curve of the 6-stage ICIP device operating at room temperature illuminated with a 1550 nm laser.

Chapter 5

Conclusion

5.1 Key Findings and Conclusions

The radiometric and noise results contained in this work reveal a number of different findings for those who design, test, and operate photovoltaic infrared detector. One of the most clear findings is that the noise estimation technique which includes only the shot noise and Johnson noise of a detector has limited utility in determining the actual device performance. This was proved to be especially true for devices with high G-R and tunneling currents such as in the case of the irradiated nBn detector. The nBn detector noise matched the estimated noise well where the current was diffusion limited but demonstrated noise multiple orders of magnitude higher than predicted after radiation exposure. This should be considered in evaluating device's radiation tolerance where in addition to monitoring the quantum efficiency degradation and the dark current increase, the noise can increase more than predicted and limit the device performance even more.

An additional finding was the dominance of $1/f$ noise in the LWIR ICIP detectors tested in this work. The high $1/f$ noise seemed to eliminate the possibility of prob-

ing the noise gain theory directly. The high dark current and low external quantum efficiency ICIPs made it difficult to operate the devices in circumstances where the photocurrent was significant compared to the dark current which was seen as a prerequisite to elevating the shot noise above the other noise sources. The series of noise tests in combination with the dark current Arrhenius analyses performed, however, did reveal a strong correlation between the G-R current and the $1/f$ noise. This finding was consistent with the results shown for the nBn devices. At a minimum, this provides a starting point for reducing the $1/f$ noise of future devices. Beyond that, the finding that the $1/f$ noise did not strongly correlate to either the diffusion current or the temperature-independent current processes, disproved the hypothesis that since the ICIP device architecture necessitates tunneling as a key mechanism of carrier transport that the ICIP devices might always be limited by $1/f$ noise.

With regard to the negative differential conductance of the ICIP devices, this work drew important ties to the physics of resonant tunneling diodes. The results contained herein showed the clear affect the negative conductance has on circuit stability which in part helps validate the theories proposed linking the NDC features to resonant tunneling through the barriers. The laser illumination experiments, however, uncovered potential inconsistency in the theory that the resonant tunneling occurs in the electron barrier, supporting in some ways claims in the literature that the resonant tunneling leading to the NDCs occurs in the hole barriers. Beyond contributing experimentally to theories about the physical origins of the NDC features, this work revealed the potential difficulties and advantages of operating the ICIP devices at biases near the NDC peaks. This work also showed that the NDC peaks could be used as indicators of the bias distribution among the different stages of the ICIP devices. The results produced from illuminating the ICIP with lasers of different wavelengths showed that the current mismatch between stages does appear to create electrical gain wherein different biases are induced in the different stages in order to preserve current continuity.

5.2 Recommended Future Work

The findings above immediately motivate additional research surrounding ICIP devices. The most obvious experiment would be to substitute MWIR or even SWIR ICIP detectors for the LWIR used in the this work and repeat the noise analysis with varying temperatures, biases, and illumination levels. While not certain, this would result in a lower dark current to photocurrent ratio that would make the photocurrent-induced shot noise more distinguishable and might make it possible to calculate the gain and validate or invalidate the proposed gain theory of multi-stage ICIPs.

The laser illumination experiments drew attention to additional questions that need to be answered about the physical origin of the NDCs, namely where the resonant tunneling occurs and how it is affected by bias. Additional work is recommended to more fully explore these questions. Beyond that, results presented herein only begin to explore the utility of the photocurrent gain caused by the NDC of the ICIP devices. It would be worthwhile to explore methods of optimizing this gain and for finding applications in which it might prove to be useful. One can theorize that the photocurrent could be maximized by determining the distribution of stages necessary for a particular illumination scheme that would shift the peak in the illuminated IV curve over the valley in the unilluminated IV curve. This may provide, at that specific bias, a maximized photocurrent gain. In parallel or after the photocurrent gain proved useful, an additional study could be undertaken to shift the peak in the photocurrent gain to lower biases. If there is an application that could make practical use of the photocurrent gain, this would allow the device to operate at a lower bias to conserve power.

In addition to the specific findings of this work, it should be noted that along the way, major improvements were made in the specific test apparatus used with regard

to allowing calibrated radiometric testing in the noise dewar and in automating the collection of noise spectra for varying temperatures and biases through LabView control. This capability should be employed for exploring the noise of IR detectors with differing materials and architectures.

References

[1] Eugene Hecht. *Optics*. Pearson Education, Inc., San Fransico, CA, second edition, 2002.

[2] J.D. Vincent. *Fundamentals of Infrared Detector Operation and Testing*. Wiley-Interscience, New York, 1990.

[3] E. L. Dereniak and G. D. Boreman. *Infrared Detectors and Systems*. John Wiley & Sons, Inc., New York, first edition, 1996.

[4] S. M. Sze. *Physics of Semiconductor Devices*. Wiley-Interscience, New York, second edition, 1981.

[5] Richard Muller and Theodore Kamins. *Device Electronics for Integrated Circuits*. Wiley, New York, third edition, 2003.

[6] K. F. Brennan and C. J. Summers. Theory of resonant tunneling in a variably spaced multiquantum well structure: An Airy function approach. *Journal of Applied Physics*, 61(2):614–623, 1987.

[7] S. Maimon and G. W. Wicks. nBn detector , an infrared detector with reduced dark current and higher operating temperature. *Appl. Phys. Lett.*, 89:1511091–1511093, 2006.

[8] Jian V. Li, Rui Q. Yang, Cory J. Hill, and Shun Lien Chuang. Interband cascade detectors with room temperature photovoltaic operation. *Appl. Phys. Lett.*, 86(101102):1–3, 2005.

[9] Robert T. Hinkey and Rui Q. Yang. Theory of multiple-stage interband photovoltaic devices and ultimate performance limit comparison of multiple-stage and single-stage interband infrared detectors. *Journal of Applied Physics*, 104506(May), 2013.

[10] Robert T. Hinkey and Rui Q. Yang. Comparison of ultimate limits of interband cascade infrared photodetectors and single-absorber detectors. In *Infrared Sensors, Devices, and Applications III*, volume 8868, pages 1–10, 2013.

[11] Geoffrey D. Jenkins, Christian P. Morath, and Vincent M. Cowan. Empirical Study of the Disparity in Radiation Tolerance of the Minority-Carrier Lifetime Between II VI and III V MWIR Detector Technologies for Space Applications. *Journal of Electronic Materials*, 46(9):5405–5410, 2017.

[12] Christian P. Morath, Vincent M. Cowan, Laura A. Treider, Geoffrey D. Jenkins, and John E. Hubbs. Proton irradiation effects on the performance of III-V-based, unipolar barrier infrared detectors. *IEEE Trans. Nucl. Sci*, 62(2):512–519, 2015.

[13] Lin Lei, Lu Li, Hao Ye, Hossein Lotfi, Rui Q. Yang, Matthew B. Johnson, Jeremy A. Massengale, D. Tetsuya, and Michael B. Santos. Long wavelength interband cascade infrared photodetectors operating at high temperatures. *Journal of Applied Physics*, 120(193102):1–14, 2016.

[14] J. Piotrowski, P. Brzozowski, and K. Jozwikowski. Stacked multijunction photodetectors of long-wavelength radiation. *Journal of Electronic Materials*, 32(7), 2003.

[15] H. Schneider and H.C. Liu. *Quantum Well Infrared Photodetectors*. Springer, New York, 2006.

[16] H. C. Liu. Photoconductive gain mechanism of quantum-well intersubband infrared detectors. *Appl. Phys. Lett.*, 60(1992):1507–1509, 1992.

[17] W. A. Beck. Photoconductive gain and generation-recombination in multiple-quantum-well infrared detectors. *Appl. Phys. Lett.*, 63(26):3589–3592, 1993.

[18] B. F. Levine, A. Zussman, S. D. Gunapala, M. T. Asom, J. M. Kuo, and W. S. Hobson. Photoexcited escape probability, optical gain , and noise in quantum well infrared photodetectors. *Journal of Applied Physics*, 72(1992):4429–4442, 1992.

[19] C. Schonbein, H. Schneider, R. Rehm, and M. Walther. Noise gain and detectivity of n-type GaAs/AlAs/AlGaAs quantum well infrared photodetectors. *Applied Physics Letters*, 73(9):1251–1253, 1998.

[20] Jerry M. Olson and Sarah R. Kurtz. Current-matched, high-efficiency, multijunction monolithic solar cells, 1993.

[21] Wenxiang Huang, Lin Lei, Lu Li, Jeremy A. Massengale, Rui Q. Yang, Tetsuya D. Mishima, and B. Michael. Current-matching versus non-current-matching in long wavelength interband cascade infrared photodetectors. *Journal of Applied Physics*, 122(083102), 2017.

[22] Rui Q. Yang, Wenxiang Huang, Lu Li, Lin Lei, Jeremy A. Massengalea, Tetsuya D. Mishima, and Michael B. Santos. Gain and resonant tunneling in interband cascade IR photodetectors. In *SPIE 10540, Quantum Sensing and Nano Elecronics and Photonics XV*, number January, pages 1–8, San Fransico, CA, 2018.

[23] Lin Lei, Lu Li, Wenxiang Huang, Jeremy A. Massengale, Hao Ye, Hossein Lotfi, Rui Q. Yang, D. Tetsuya, Michael B. Santos, and Matthew B. Johnson. Resonant tunneling and multiple negative differential conductance features in long wavelength interband cascade infrared photodetectors. *Appl. Phys. Lett.*, 111(113504), 2017.

[24] S. K. Diamond, E. Ozbay, M. J. W. Rodwell, D. M. Bloom, Y. C. Pao, and J. S. Harris. Resonant tunneling diodes for switching applications. *Applied Physics Letters*, 54:153–155, 1989.

[25] C. Kidner, I. Mehdi, J. R. East, and G. I. Haddad. Bias circuit instabilities and their effect on the d.c. current-voltage characteristics of double-barrier resonant tunneling diodes. *Solid-State Electronics*, 34(2):149–156, 1991.

[26] Kiochi Maezawa. Resonant tunneling diodes, 2014.

[27] Z. Tian, S. E. Godoy, H. S. Kim, T. Schuler-Sandy, J. A. Montoya, and S. Krishna. High operating temperature interband cascade focal plane arrays. *Appl. Phys. Lett.*, 105(051109):1–5, 2014.

[28] Rui Q. Yang, Zhaobing Tian, Zhihua Cai, J. F. Klem, Matthew B. Johnson, and H. C. Liu. Interband-cascade infrared photodetectors with superlattice absorbers. *Journal of Applied Physics*, 107(2010):1–6, 2010.

[29] Z. Tian, R. T. Hinkey, Rui Q. Yang, D. Lubyshev, Y. Qiu, J. M. Fastenau, W. K. Liu, and M. B. Johnson. Interband cascade infrared photodetectors with enhanced electron barriers and p -type superlattice absorbers. *Journal of Applied Physics*, 111(024510):1–6, 2012.

[30] Z. Tian, T. Schuler-Sandy, and S. Krishna. Electron barrier study of mid-wave infrared interband cascade photodetectors. *Appl. Phys. Lett.*, 103(083501):1–4, 2013.

[31] Hajime Asahi. Temperature-Insensitive Band-Gap III-V Semiconductors: Tl-III-V and III-V-Bi. In Kasap S. and P. Capper, editors, *Springer Handbook of Electronic and Photonic Materials*, chapter 23, pages 543–555. Springer, Cham, 2017.

[32] W. E. Tennant, Donald Lee, Majid Zandian, Eric Piquette, and Michael Carmody. MBE HgCdTe technology : A very general solution to IR detection , described by "Rule 07 ", a very convenient heuristic. *J. Electron. Mater.*, 37(9):1406–1410, 2008.

[33] J. B. Johnson. Thermal agitation of electricity in conductors. *Physical Review*, 32:97–108, 1928.

[34] Zhao-bing Tian and Sanjay Krishna. Mid-infrared interband cascade photodetectors with different absorber designs. *IEEE Journal of Quantum Electronics*, 51(4):1–5, 2015.

[35] Wenxiang Huang, Lu Li, Lin Lei, Jeremy A. Massengale, Rui Q. Yang, Tetsuya D. Mishima, and Michael B. Santos. Electrical gain in interband cascade infrared photodetectors. *Journal of Applied Physics*, 123(113104):1–11, 2018.

[36] R. Rehm, H. Schneider, C. Schonbein, and M. Walther. Noise current investigations of g r noise limited and shot noise limited QWIPs. *Physica E*, 7:124–129, 2000.

[37] A. Rogalski. HgCdTe infrared detector material : history , status and outlook. *Reports on Progress in Physics*, 68:2267–2336, 2005.

[38] Alexandre Brunner, Laurent Rubaldo, V. Destefanis, F. Chabuel, A. Kerlain, D. Bauza, and N. Baier. Improvement of RTS Noise in HgCdTe MWIR Detectors. *Journal of Electronic Materials*, 43(8):3060–3064, 2014.

[39] F. N. Hooge. 1/f Noise. *Physica*, 83B:14–23, 1976.

[40] Stephen P. Tobin, Shigesato Iwasa, and Timothy J. Tredwell. 1/f noise in (Hg, Cd)Te photodiodes. *IEEE Trans. Electron. Dev.*, 27(1):43–48, 1980.

[41] Y. Nemirovsky and A. Unikovsky. Tunneling and 1 / f noise currents in HgCdTe photodiodes. *J. Vac. Sci. & Tech. B*, 10(4):1602–1610, 1992.

[42] Wenmu He and Zeynep Çelik-Butler. Temperature dependence of 1 /f noise in HgCdTe MIS infrared detectors. *IEEE Transactions on Electron Devices*, 42(1):160–165, 1995.

[43] C. P. Morath. Personal Correspondence, 2018.

[44] Vincent Cowan. Personal Correspondence, 2014.

[45] S. Knotek and H. P. Gush. Cooled lownoise bolometer preamplifier. *Review of Scientific Instruments*, 48:1223–1224, 1977.

[46] E. L. Dereniak, R. R. Joyce, and R. W. Capps. Low-noise preamplifier for photoconductive detectors. *Review of Scientific Instruments*, 48(392), 1977.

[47] Vincent M. Cowan, Christian P. Morath, Stephen Myers, Nutan Gautam, and Sanjay Krishna. Low temperature noise measurement of an InAs / GaSb-based nBn MWIR detector. In *Infrared Sensors, Devices, and Applications XXXVII*, volume 8012, pages 1–8, 2011.

[48] Eli A. Garduno, Damien L. Waden, Vincent M. Cowan, and Christian P. Morath. Low-frequency noise spectrum measurements of mid-wave infrared nBn detectors with superlattice absorbers. In *SPIE 9616, Nanophotonics and Macrophotonics for Space Environ. IX*, page 96160H, 2015.

[49] Y. Livneh, P. C. Klipstein, O. Klin, N. Snapi, S. Grossman, A. Glozman, and E. Weiss. K·p model for the energy dispersions and absorption spectra of InAs/GaSb type-II superlattices. *Physical Review B - Condensed Matter and Materials Physics*, 86(23):1–16, 2012.